Available online at www.sciencedirect.com
ScienceDirect
Comput. Methods Appl. Mech. Engrg. 370 (2020) 113284
Computer methods in applied mechanics and engineering
www.elsevier.com/locate/cma

A DG-based interface element method for modeling hydraulic fracturing in porous media

Ruijie Liu[a,*], Zhijun Liu[a], Mary F. Wheeler[b]

[a] Department of Mechanical Engineering, The University of Texas at San Antonio, San Antonio, TX 78249, United States of America
[b] Center for Subsurface Modeling, Oden Institute for Computational Engineering and Sciences, The University of Texas at Austin, Austin, TX 78712, United States of America

Available online 3 August 2020

Abstract

Fracture propagation coupled with fluid flow in porous media has very important applications in fracking in oil and gas reservoirs, corrosion in ceramics, and degradation of human bones. Modeling fracture failure in porous media governed by the coupled solid and fluid field equations is challenging and time-consuming. This paper extends discontinuous Galerkin (DG) finite element methods to model crack openings in porous media through exploiting an easy construction of interfaces for potential crack paths by locally breaking continuous elements. Consequently, a finite element mesh for fracture apertures is completely and gracefully constructed using DG interface objects as well as the definitions of jumps of displacements across the DG interfaces defined for bulk matrices. Furthermore, rigid cohesive laws often adopted for crack openings can be naturally implemented in DG formulations without introducing artificial stiffness, which may eventually improve the performance for implicit formulations in handling crack openings in porous media. In this work, we perform a consistent, fully implicit, and fully coupled hybrid DG/continuous finite element formulation for three field equations including the solid, bulk fluid, and fluid in fracture apertures resulting from crack openings. We verify our DG formulation and implementation using the Khristianovich-Geertsma-DeKlerk analytical solutions. Finally, we further demonstrate a good performance of the proposed DG method by modeling fracking in an oil reservoir containing two nature fractures.

Keywords: DG; IIPG; Hydraulic fracturing; Porous media; Cohesive law; Implicit method

1. Introduction

Modeling fracture propagation in porous media has numerous important applications such as simulating fracking in oil and gas reservoirs, fracture analysis of aging human bones, and evaluation of accelerated degradation of ceramic matrix composites in aerospace shuttles. Simulating crack openings in porous media is challenging and time-consuming because it involves not only coupled fluid diffusion and solid deformation but also initiation, propagation, and branching of cracks in bulk matrices as well as fluid flowing through fracture apertures resulting from crack openings. This paper applies discontinuous Galerkin (DG) finite element methods to achieve high-fidelity simulations on fracture propagation in porous media through locally breaking continuous Galerkin (CG) finite elements.

* Corresponding author.
E-mail address: ruijie.liu@utsa.edu (R. Liu).

https://doi.org/10.1016/j.cma.2020.113284

Research effort on developing physical models and mathematical formulations for hydraulic fracturing problems has been extensively invested [1–12]. For example, Khristianovich-Geertsma-DeKlerk (KGD) and Perkins-Kern-Nordgren (PKN) plane strain crack models were proposed and an axial symmetric crack model was developed in [13] by assuming the incompressibility of injected fluids and linear elasticity of solid skeletons. These hydraulic fracture models can be solved analytically and four special asymptotic solutions [9,10] including storage-viscosity, storage-toughness, leak-off-viscosity, and leak-off-toughness [5,6,8,11] were derived. These four special asymptotic solutions have been selected as benchmarks for verification of numerical methods formulated for solving more general and complex crack propagations in permeable solids.

Numerical techniques well developed for modeling crack openings in pure solids have been extended to simulate hydraulic fracture problems. These techniques may be categorized into four main methods including Nodal Force Releasing [14], Cohesive Zone Method (CZM) [15–19], Extended Finite Element Method (XFEM) [20], and Phase-Field Method [21]. In [22,23], a remesh solver was developed to split nodes or add new nodes on potential crack paths to accommodate the openings of cracks. In these formulations, nodes on opened crack surfaces are applied by fluid pressure and nodal forces are released once tractions on interfaces exceed material cohesive strengths or pressure-dependent cohesive strengths. The dominated numerical framework for modeling hydraulic fracture problems is the CZM method [22,24–30]. In this technique, cohesive zone elements are preconstructed along potential crack paths and crack openings are realized by the use of the softening behavior of CZM elements governed by material cohesive laws. In general, hydraulic fracture problems may be solved fast using CZM if nonlinear iterations converge. In modeling fracture propagation in linear elastic porous media, good agreements between predictions from this method and analytical solutions for the single plane strain/axial symmetric crack with regard to both storage-viscosity and storage-toughness models have been reported in [29]. Researchers in [30–32] had reported their XFEM formulations and good verification results using plane strain/axial symmetric hydraulic fracturing benchmarks. Recently, phase-field methods have been exploited to model hydraulic fracturing problems in porous media.

However, the nodal force release method, in general, has challenges in achieving complete simulations using implicit formulations for highly nonlinear problems. The limitations of other three methods were well discussed. Crack openings can be improved by inserting interface elements along with cohesive laws in front of crack tips. However, the spurious compliance stiffness introduced into CZM elements brings a numerical issue in accurately computing stresses around crack tips. On the other hand, constructing CZM or CZM-based XFEM elements is time-consuming especially for hydraulic fracture problems. Finally, while the phase-field method has a great potential in modeling hydraulic fracturing problems, an accurate computation of stresses around cracks and a considerable effort on substantial verifications of cracking opening displacements using hydraulic fracture benchmarks, i.e. the KGD models are highly expected. In this paper, we apply DG methods to efficiently model hydraulic fracturing problems by exploiting the excellent feature of DG methods in generating crack interfaces.

By introducing a jump in primary field variables and an average on flux-like field variables across interfaces among broken elements, DG methods [33–36] have been formulated to solve fluid flow problems as well as solid mechanics problems. The Symmetric Interior Penalty Galerkin (SIPG), Non-symmetric Interior Penalty Galerkin (NIPG), Non-symmetric Galerkin without penalty (OBB, i.e. Oden–Babuska–Baumann), and Incomplete Interior Penalty Galerkin (IIPG) have been further developed in [37–44] for either pure fluid flow fields such as the Navier–Stokes equation or pure solid mechanics fields such as nearly incompressible elasticity or plasticity problems. Nonphysical oscillatory pore pressure and temperature solutions obtained from continuous elements for coupled solid, fluid, and temperature field poromechanics problem can be avoided using DG methods [43,45,46]. Specifically, It should be noted that a full DG discretization for a whole model results in an explosion in unknowns, which is not practical. However, for crack problems, the explosion in unknowns can be avoided by only applying DG elements to areas where cracks may have potentials to develop. DG formulations were extended in modeling crack propagation for linear elastic materials in [47,48], composite materials in [49,50], and damaging materials in, and ductile fracture propagation in [51,52].

We now discuss a few contributions of this paper. First, while recently, DG methods have been formulated to model crack opening problems [49,51,52], they have been little studied for hydraulic fracturing problems. In this paper, we invested an effort on extending DG methods to the field of modeling crack openings in permeable solids filled with fluids. We note that the construction of finite element meshes is a very complex and time-consuming task for fracture mechanics problems. Furthermore, it is even more challenging in modeling crack openings in

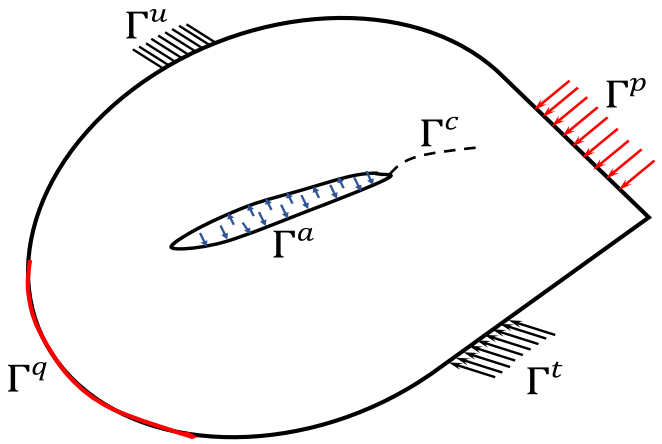

Fig. 1. Hydraulic fracturing problem: Domain of porous medium and boundaries.

porous media where the coupling effects among the deformation of the solid skeleton, the flow of the fluid in the bulk matrix, and the fluid flow in varied fracture apertures must be carefully handled. We underline that the numerical algorithms in constructing broken elements in DG methods have been already established. For example, as demonstrated in [51,52], the interior interfaces can be efficiently placed on potential crack paths by simply grouping continuous elements on crack paths into two element sets. These two sets of elements are further broken into DG meshes. From the mesh construction point of view, the setup of element sets by grouping elements in continuous meshes by users is much easier than inserting nodes/elements into continuous meshes. More precisely, the issue of time-consuming for CZM methods can be much avoided. Second, by adopting DG methods we are able to gracefully enforce the so called rigid cohesive laws, i.e. more physics-based fracture energy failure models that have been studied in [49,50] for fracture propagation in pure solids. The artificially introduced stiffness in traditional CZM models are avoided in such rigid cohesive models. We articulate that the adoption of rigid cohesive laws is critical to modeling fluid flow in fracture apertures as the introduction of artificial initial thicknesses required in traditional CZM elements is saved. Third, other than applying other DG methods, we adopted the IIPG for hydraulic fracturing problems. This is because the success in modeling coupled solid and fluid flow field problems has been achieved only in the IIPG formulation for porous media [43,46]. Finally, we perform a fully coupled and fully implicit IIPG formulation for finite deformation problems by consistently linearizing highly nonlinear coupled equations. This high nonlinearity results from a nonlinear cubic flow law for fluid flow within fracture apertures that is a function of the thicknesses of apertures, a large opening of fractures, and an implicitly applied pressure loading on fracture wall surfaces. Specifically, the tangent stiffness contributed from the pressure loading on fracture surfaces must be carefully derived for any implicit methods.

Finally, we outline our presentation for each section in this paper. Section 2 summarizes the coupled three-field governing equations including the solid, fluid in bulk matrix, and injected fluid in apertures for hydraulic fracturing problems. Rigid cohesive laws for crack openings and a lubricating theory for fluid flow in narrow apertures are discussed. We make a mathematical statement for the IIPG weak formulation for hydraulic fracturing problems in Section 3. In this section, we perform a consistent linearization for the stated nonlinear IIPG weak equations. We discuss the implementation of the IIPG method in Section 4. Specifically, we present an innovative construction for fluid flow in apertures by exploiting well defined DG data structures. In Section 5, first, we verify our DG formulation by solving a KGD benchmark. We then demonstrate a good performance of our IIPG formulation by modeling a more complex fracturing problem having two natural fractures embedded in an oil reservoir. Conclusions are summarized in Section 6.

2. Coupled governing equations

Physical events of hydraulic fracturing in porous media involve the initiation, opening, and propagation of cracks, the deformation of solid skeletons, the flow of fluids in bulk solid matrices, and the flow of fluids within the

existing apertures or new apertures induced from crack openings due to fluid injection. First, the deformation of solid skeleton coupled with the fluid pressure diffusion in porous media without discontinuities can be addressed by the geomaterial consolidation theory. In Biot's consolidation theory, the solid deformation equation is coupled with fluid pressure diffuse equation by decomposing the total stress into the effective stress taken by the solid skeleton and the hydro-pressure associated with fluids filled in pores. This implies that in general, the drawdown of reservoir pressure due to fluid depletion induces reservoir compaction and ground surface subsidence due to the increase in the effective stress for reservoir rock skeletons. Second, for the cases of porous media with apertures, the flowing of fluids within apertures in addition to fluid flow in bulk matrices can be simplified into cases of fluid flow through the Poiseuille's parallel plate [53] where an equivalent permeability was derived for fluid flow within apertures. Third, variation of apertures in their thicknesses and lengths affects fluid flow in fracture apertures and injection of fluids into apertures drives the increase in fluid pressure that acts as an external pressure loading for solid skeletons. Finally, the increase in fluid pressure in apertures may eventually results in solid skeleton failure in terms of the initiation and propagation of fractures. For hard porous media, the most popular fracture model is based on linear elastic fracture mechanics theories where the initiation of crack openings is governed by fracture energy indices or cohesive laws. In this section, we construct a mathematical statement for hydraulic fracturing problems by introducing a few notations and variables.

First, as shown in Fig. 1, we categorize the whole boundary of a porous medium body occupying a domain $\boldsymbol{\Omega}$ into an exterior boundary set $\boldsymbol{\Gamma}$ and an interior boundary set $\boldsymbol{\Gamma}^a$ where the superscript a indicates the boundary surfaces related to the discontinuities within the porous medium that may include apertures or wellbores. With regard to the solid field, we denote $\boldsymbol{\Gamma}^u \cup \boldsymbol{\Gamma}^t = \partial\boldsymbol{\Omega}$ as the displacement and the traction boundary portions, respectively. Furthermore, we partition the traction boundary $\boldsymbol{\Gamma}^t$ into the exterior traction boundary $\boldsymbol{\Gamma}^{t/a}$ and the interior traction boundary of apertures $\boldsymbol{\Gamma}^a$. For fluid flow in bulk matrices, we denote the prescribed pore pressure boundary as $\boldsymbol{\Gamma}^p$ and fluid flux boundary as $\boldsymbol{\Gamma}^q$. We denote u as the primary displacement variable for the solid deformation and $\boldsymbol{p}$ for the primary pressure variable for both fluid flow in bulk matrices and in apertures. Specifically, noting that a newly created interior surface due to fracture propagation is also a key part of solutions, we define this new crack surface as $\boldsymbol{\Gamma}^c$. The aperture of fracture $\boldsymbol{w_a}$ on $\boldsymbol{\Gamma}^a \cup \boldsymbol{\Gamma}^c$ is also the interested solution. We assume that apertures are narrow and the domain of apertures can be defined by $\boldsymbol{\Omega_a} = \boldsymbol{S_a} \times \boldsymbol{w_a}$ where S_a the middle surface of apertures that can be further defined by two wall surfaces of apertures. The injection rate is denoted by $\boldsymbol{Q_a}$ in apertures. We now construct a mathematic statement of the problem for hydraulic fracturing in porous media as follows:

Find $(\mathbf{u}(x,t) \in \boldsymbol{\Omega}/\boldsymbol{\Omega_a}, \mathbf{p}(x,t) \in \boldsymbol{\Omega}, \mathbf{w_a} \in \boldsymbol{\Omega} \cap \boldsymbol{\Omega_a})$ **that satisfy**:

$$\begin{cases} \nabla \cdot \boldsymbol{\sigma}(x,t) + \mathbf{f}(x,t) = \mathbf{0} & (x,t) \in \boldsymbol{\Omega}/\boldsymbol{\Omega_a} \times (\mathbf{0}, \infty) \\ \boldsymbol{\alpha}\dot{\boldsymbol{\epsilon}}_v(x,t) + \frac{1}{M}\dot{\boldsymbol{p}}(x,t) + \nabla \cdot \boldsymbol{q}k(x,t) = \boldsymbol{s_q}(x,t) & (x,t) \in \boldsymbol{\Omega}/\boldsymbol{\Omega_a} \times (\mathbf{0}, \infty) \\ \dot{\boldsymbol{w}}_a(x,t) + \nabla \cdot \boldsymbol{q}_a(x,t) = \boldsymbol{Q_a}\boldsymbol{w_a}(x,t) & (x,t) \in \boldsymbol{S_a} \times (\mathbf{0}, \infty) \end{cases} \tag{1}$$

with boundary conditions:

$$\begin{cases} \boldsymbol{u}(x,t) = \bar{\boldsymbol{u}}(x,t) & x \in \boldsymbol{\Gamma}^u \times (\mathbf{0}, \infty); \\ \boldsymbol{\sigma}(x,t)\boldsymbol{n}(x,t) = \bar{t}_s(x,t) & x \in \boldsymbol{\Gamma}^{t/a} \times (\mathbf{0}, \infty); \\ \boldsymbol{\sigma}(x,t)\boldsymbol{n}(x,t) = -\bar{\boldsymbol{p}}(x,t)\boldsymbol{n}(x,t) & x \in \boldsymbol{\Gamma}^a \times (\mathbf{0}, \infty); \\ \boldsymbol{p}(x,t) = \bar{\boldsymbol{p}}(x,t) & x \in \boldsymbol{\Gamma}^p \times (\mathbf{0}, \infty); \\ \boldsymbol{q}(x,t) \cdot \boldsymbol{n}(x,t) = \bar{\boldsymbol{q}}(x,t) & x \in \boldsymbol{\Gamma}^q \times (\mathbf{0}, \infty); \\ \boldsymbol{q}_a(x,t) \cdot \boldsymbol{n}(x,t) = \bar{\boldsymbol{q}}_a(x,t) & x \in \boldsymbol{\Gamma}^a \times (\mathbf{0}, \infty). \end{cases} \tag{2}$$

and initial conditions:

$$\begin{cases} \boldsymbol{\sigma}(x,t)|_{t=0} = \boldsymbol{\sigma_0}(x) & x \in \boldsymbol{\Omega}/\boldsymbol{\Omega_a}; \\ \boldsymbol{p}(x,t)|_{t=0} = \boldsymbol{p_0}(x) & x \in \boldsymbol{\Omega}/\boldsymbol{\Omega_a}; \\ \boldsymbol{p}(x,t)|_{t=0} = \boldsymbol{p_{0a}}(x) & x \in \boldsymbol{S_a}. \\ \boldsymbol{w_a}(x,t)|_{t=0} = \boldsymbol{w_{0a}}(x) & x \in \boldsymbol{\Omega} \cap \boldsymbol{\Omega_a}. \end{cases} \tag{3}$$

where $\boldsymbol{\sigma}$, $\boldsymbol{f}$, $\boldsymbol{p}$, $\boldsymbol{q}$, $\boldsymbol{q_a}$, $\boldsymbol{s_q}$, and $\boldsymbol{Q_a}$ are the Cauchy stress, body force of total porous media, pore pressure or fluid pressure in apertures, flow velocity in bulk matrix, flow velocity in apertures, flow source in bulk matrices, and fluid injection rate in apertures. Parameters $\boldsymbol{\alpha}$ and $\boldsymbol{M}$ in Eq. (1) are the Biot coefficient and modulus. They are further functions of the solid skeleton bulk modulus (k_b), solid grain bulk modulus ($\boldsymbol{k_s}$), fluid bulk modulus ($\boldsymbol{k_f}$), and porosity ($\boldsymbol{\phi}$) of porous media defined as follows:

$$\begin{cases} \boldsymbol{\alpha} = \mathbf{1} - \frac{k_b}{k_s}; \\ \boldsymbol{M}(x,t) = \frac{k_s k_f}{k_f(\alpha - \phi(x,t)) + k_s \phi}(x,t). \end{cases} \tag{4}$$

$\boldsymbol{f}$ in the first equation in Eq. (1), the body force of porous media, is function of the porosity, densities ($\boldsymbol{\rho_f}$ and $\boldsymbol{\rho_s}$) of fluids and solid skeletons, and the gravity vector ($\boldsymbol{g}$) as follows:

$$\boldsymbol{f}(x,t) = [(\mathbf{1} - \boldsymbol{\phi})\boldsymbol{\rho_s} + \boldsymbol{\phi}\boldsymbol{\rho_f}]\boldsymbol{g} \tag{5}$$

where $\boldsymbol{g} = (0, 0, -g)$ and g is the gravity of the acceleration if the coordinate z along the upward direction for reservoir problems. Coupled Eq. (1) must be solved with the solid kinematic condition, constitutive laws associated to solids and fluids, and crack opening criteria summarized as follows:

(a) Relation between Strain and Displacement—Kinematic Condition for Infinitesimal Strain:

$$\boldsymbol{\epsilon} = \frac{\mathbf{1}}{\mathbf{2}}(\nabla \boldsymbol{u} + \nabla^T \boldsymbol{u}). \tag{6}$$

where ϵ is the second-order strain tensor and notation ∇ is the gradient operator with respect to current coordinates.

(b) Constitutive Law—Elasticity Model for Solid Skeletons

$$\boldsymbol{\sigma}'' = \boldsymbol{\mathcal{C}}\boldsymbol{\epsilon} \tag{7}$$

where $\boldsymbol{\mathcal{C}}$ is the fourth-order elasticity tensor, $\boldsymbol{\sigma}''$ the effective stress tensor, and $\boldsymbol{\epsilon}$ the elastic strain tensor. The relation between the effective stress $\boldsymbol{\sigma}''$ and total stress $\boldsymbol{\sigma}$ is written as follows:

$$\boldsymbol{\sigma}'' = \boldsymbol{\sigma} - \boldsymbol{\alpha}\boldsymbol{p} \tag{8}$$

(c) Constitutive Law—Darcy Law for Fluid flow in Bulk Porous Media:

$$\boldsymbol{q} = -\boldsymbol{D}^f(\nabla \boldsymbol{p} - \boldsymbol{f}^f) = -\frac{\boldsymbol{\mathcal{K}}}{\boldsymbol{\mu}}(\nabla \boldsymbol{p} - \boldsymbol{\phi}\boldsymbol{\rho_f}\boldsymbol{g}). \tag{9}$$

where $\boldsymbol{D}^f$ is the second-order conductivity tensor that can be defined in terms of the second-order permeability tensor $\boldsymbol{\mathcal{K}}$ and viscosity $\boldsymbol{\mu}$.

(d) Constitutive Law—Lubricating Theory for Fluid Flow within Apertures:

$$\boldsymbol{q_a} = -\boldsymbol{D}^a \nabla \boldsymbol{p}. \tag{10}$$

where $\boldsymbol{D}^a$ is the second-order conductivity tensor for a general 3D fracture aperture channel flow illustrated in Fig. 2. The conductivity tensor can be further locally defined in terms of the thickness (w_a) of fracture apertures and the viscosity $\boldsymbol{\mu}$ as follows:

$$\boldsymbol{D}^a = \begin{pmatrix} \boldsymbol{k_a} & \mathbf{0} & \mathbf{0} \\ \mathbf{0} & \boldsymbol{k_a} & \mathbf{0} \\ \mathbf{0} & \mathbf{0} & \mathbf{0} \end{pmatrix} \tag{11}$$

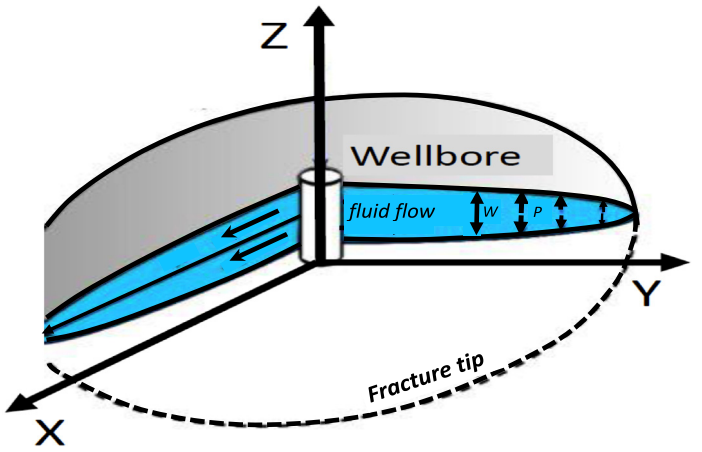

Fig. 2. Fluid flow in 3D aperture channels where permeability tensors are locally defined.

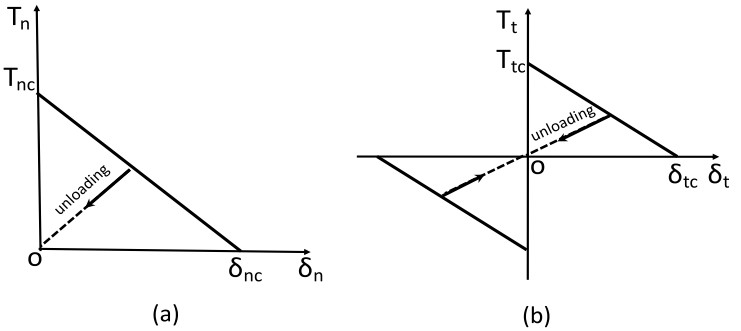

Fig. 3. Illustration of a rigid cohesive law model: (a) Mode I and (b) Mode II.

where $\boldsymbol{k_a} = \frac{w_a^3}{12\mu\eta}$ is the fracture permeability experimentally validated in [53] and $\boldsymbol{\eta}$ varies from **1.04** to **1.65** taking account into the non-parallel surface effect.

(d) Crack Opening Criteria—Fracture Energy Release Rate/Cohesive Law:

Stress, strain, and energy-based material failure models have been developed for fracture initiation and propagation in solid media. Among these models, the fracture energy release based cohesive law is popular in modeling linear elasticity fracture mechanics problems. This cohesive model was proposed in [19,26] to simulate crack opening by gradual reduction in traction on cracking surfaces. In the model, the stress singularity at crack tips is avoided for linear elastic solids. Furthermore, the so called rigid cohesive laws [15] are often adopted to avoid an artificial stiffness setup required in the conventional cohesive laws before cracking. Fig. 3(a) and (b) illustrate the softening behavior of a linear rigid cohesive model for Mode I and Mode II cracks, respectively. In Fig. 3(a), $\boldsymbol{T_n} = (\boldsymbol{\sigma}''\boldsymbol{n^c}) \cdot \boldsymbol{n^c}$ is the normal component of the traction on an interface with its normal directional vector $\boldsymbol{n^c}$, $\boldsymbol{\delta_n} = [\boldsymbol{u}] \cdot \boldsymbol{n^c}$ the crack opening displacement (COD) of apertures where $[\boldsymbol{u}]$ is the displacement jump across a crack, $\boldsymbol{T_{nc}}$ the critical tensile strength at which material softening starts, and $\boldsymbol{\delta_{nc}}$ the critical COD at which materials completely lost tensile stiffness. In Fig. 3(b), $\boldsymbol{T_t} = \boldsymbol{\sigma}''\boldsymbol{n^c} - \boldsymbol{T_n}\boldsymbol{n^c}$ is the tangent component of the traction on the interface, $\boldsymbol{T_{nt}}$ the critical shear strength, and $\boldsymbol{\delta_{nt}}$ the critical tangent displacement at which materials completely lost shear stiffness. For a more general mixed mode cohesive law, we follow our mixed rigid cohesive law in [15] where a cohesive law for a mixed mode of cracks is formulated in terms of the damage parameter of $\boldsymbol{d}$ as follows:

(1) The softening behaviors are written as follows:

$$\begin{cases} \boldsymbol{T_n} = \boldsymbol{T_{nc}}(\mathbf{1} - \boldsymbol{d}); \\ \\ \boldsymbol{T_t} = \boldsymbol{T_{tc}}(\mathbf{1} - \boldsymbol{d}). \end{cases} \tag{12}$$

where d can be defined as follows:

$$\boldsymbol{d} = \sqrt{(\frac{\boldsymbol{\delta_n}}{\boldsymbol{\delta_{nc}}})^2 + \boldsymbol{\gamma}(\frac{\boldsymbol{\delta_t}}{\boldsymbol{\delta_{tc}}})^2} \tag{13}$$

where γ is a mode-mixity coefficient or weighting parameter to serve a reduction on damage contribution from the shear mode.

(2) The critical fracture energies are computed as follows:

$$\begin{cases} \boldsymbol{G_{nc}} = \frac{1}{2}\boldsymbol{T_{nc}}\boldsymbol{\delta_{nc}} \\ \\ \boldsymbol{G_{tc}} = \frac{1}{2}\boldsymbol{T_{nt}}\boldsymbol{\delta_{tc}}. \end{cases} \tag{14}$$

where $\boldsymbol{G_{nc}}$ and $\boldsymbol{G_{tc}}$ are the normal and tangent critical fracture energies.

(3) The normal and tangent fracture energies ($\boldsymbol{G_n}, \boldsymbol{G_t}$) released at any COD level are calculated as follows:

$$\begin{cases} \boldsymbol{G_n} = \int \boldsymbol{T_n} \boldsymbol{d\delta_n} \\ \\ \boldsymbol{G_t} = \int \boldsymbol{T_t} \boldsymbol{d\delta_t}, \end{cases} \tag{15}$$

and finally,

(4) The initiation of material damage under a mixed mode is identified by:

$$\boldsymbol{T_n^2} + \boldsymbol{\gamma}\boldsymbol{T_t^2} = \boldsymbol{\sigma_0^2} \tag{16}$$

where $\boldsymbol{\sigma_0}$ is the fracture stress.

3. DG weak formulation

In this section, we perform a fully coupled and fully implicit hybrid DG/CG formulation for the three coupled field equations in Eq. (1) for hydraulic fracturing problems in deformable and permeable media. Continuous elements will be formulated for the majority of bulk matrix and DG elements will be only adaptively used in the areas around potential crack paths. It should be noted that we apply CG elements for fluid flow in fracture apertures. Furthermore, for soft rock formations or human aging bones solid phases often undergo large deformation during crack propagation. To gain the capability of modeling large openings of cracks in porous media undergoing large deformation, we implement our hybrid DG/CG formulations for these three field equations in the updated Lagrange and co-rotational finite element framework [54–56]. More precisely, we formulate our DG methods for the solid field equation of porous media in the hypo-elasticity framework by following the work in [44]. In [43,45,46], a poromechanics problem involving coupled solid, fluid flow, and thermal fields has been formulated and solved using DG methods for the case of solids undergoing small deformation. In [44], for pure solids undergoing finite deformation, DG formulations were performed and verified for both hypoelastoplasticity and hyperelastoplasticity problems. While all DG methods could be proposed to solve this hydraulic fracturing problem, we adopt the Incomplete Interior Penalty Galerkin (IIPG) [38] as this IIPG scheme exhibits a more robust performance in solving nearly incompressible elasticity problems [42] and a mathematically complete and consistent formulation can be nicely achieved for plasticity problems using this method in [44]. Moreover, the success of DG formulations is only observed in the IIPG scheme for poromechanics problems where the solid and fluid flow fields are coupled [43,46]. In this paper, we follow the IIPG scheme developed for the coupled three field poromechanics in [43] where the impact of the complexity of the coupled field equations, i.e. the coupled total stress and the Biot's stress, i.e. the effective stress on the DG formulation was properly addressed.

Finally, we underline that the newly created apertures not only bring a challenge for constructing finite element meshes to efficiently accommodate crack opening events but also bring a challenging task for implicit finite element formulations that take into account the impact of the opened crack surfaces on both solid and flow fields. More precisely, from the solid field of point view, the flow of fluids in fractured channels due to the injection of fluids exerts an external pressure loading to the solid body. For implicit formulations for large deformation of solids, to achieve converged (nonlinear Newton's iteration) solutions at a high magnitude of pressure loadings, a consistent

linearization for the pressured interior surfaces that takes into account the contribution to the tangent stiffness from pressured surfaces is required [44]. It should be mentioned that this is the case for hydraulic fracturing in oil/gas reservoirs where reservoir pore pressures are often up to 3000 to 8000 psi and pressures of injecting fluids required to generate fractures exceed reservoir pore pressures , i.e. the exerted pressure loading on fracture surfaces is extremely high. In this work, to handle this challenging for high pressure loadings from crack openings, we also perform a consistent linearization for pressure loading applied on fracture surfaces by referring the numerical scheme developed in [44,51,52] for DG interfaces undergoing finite deformation. In the following, we first make a mathematical statement of the IIPG weak formulation for coupled three field hydraulic fracturing problems. We then discuss a few unique features of this IIPG in modeling hydraulic fracturing.

3.1. Problem statement of IIPG weak formulation

For weak formulations, we define the trial space for displacement for solid field equation and the trial space for pore pressure field equation as follows:

$$\begin{cases} \mathcal{U} = \{\, \boldsymbol{u} :\ \boldsymbol{u} \in \boldsymbol{H}^{\mathbf{1}}(\Omega/\Omega),\ \boldsymbol{u}|_{\Gamma^u} = \bar{\boldsymbol{u}}\}; \\ \\ \mathcal{P} = \{\, \boldsymbol{p} :\ \boldsymbol{p} \in \boldsymbol{H}^{\mathbf{1}}(\Omega),\ \boldsymbol{p}|_{\Gamma^p} = \bar{\boldsymbol{p}}\}. \end{cases} \tag{17}$$

The test spaces for displacement, pore pressure or flow pressure in apertures are defined as follows:

$$\begin{cases} \mathcal{U}^{\mathcal{T}} = \{\, \boldsymbol{\delta u} :\ \boldsymbol{\delta u} \in \boldsymbol{H}^{\mathbf{1}}(\Omega),\ \boldsymbol{\delta u}|_{\Gamma^u} = \mathbf{0}\}; \\ \\ \mathcal{P}^{\mathcal{T}} = \{\, \boldsymbol{\delta p} :\ \boldsymbol{\delta p} \in \boldsymbol{H}^{\mathbf{1}}(\Omega),\ \boldsymbol{\delta p}|_{\Gamma^p} = \mathbf{0}\}. \end{cases} \tag{18}$$

We discretize time implicitly using the backward Euler method for flow in bulk matrices and apertures. For DG formulations, for the solid field we define:

$$\begin{cases} [\boldsymbol{u}] = (\boldsymbol{u}^{\boldsymbol{L}} - \boldsymbol{u}^{\boldsymbol{R}}); \\ \\ \{\boldsymbol{\sigma}'' \boldsymbol{n}^{\boldsymbol{L}}\} = (\boldsymbol{\sigma}^{L''} + \boldsymbol{\sigma}^{R''})\boldsymbol{n}^{\boldsymbol{L}}/\mathbf{2}. \end{cases} \tag{19}$$

where $[\boldsymbol{u}]$, $\{\boldsymbol{\sigma}'' \boldsymbol{n}^{\boldsymbol{L}}\}$, $\boldsymbol{n}^{\boldsymbol{L}}$ are the jump on the displacement across interfaces, the average on the effective traction on interfaces, the normal direction vector on the interface that is always computed from the left surface in a DG interface. Superscripts $\boldsymbol{L}$ and $\boldsymbol{R}$ indicate variables associated with the left and right surfaces in a DG interface shared by a pair of elements, i.e. the left element and right element, respectively. For the fluid flow in the bulk matrix, we define:

$$\begin{cases} [\boldsymbol{p}] = (\boldsymbol{p}^{\boldsymbol{L}} - \boldsymbol{p}^{\boldsymbol{R}}); \\ \\ \{\boldsymbol{q} \cdot \boldsymbol{n}^{\boldsymbol{L}}\} = (\boldsymbol{q}^{\boldsymbol{L}} + \boldsymbol{q}^{\boldsymbol{R}}) \cdot \boldsymbol{n}^{\boldsymbol{L}}/\mathbf{2}. \end{cases} \tag{20}$$

where $[\boldsymbol{p}]$, $\{\boldsymbol{q} \cdot \boldsymbol{n}^{\boldsymbol{L}}\}$ are the jump on the pressure across the interface, the average fluid flux on the interface. We also define $\boldsymbol{S_I}$ as the set of DG interfaces (interior interfaces). With the DG jump notations introduced in Eq. (19), variable $\boldsymbol{w_a}$, the thickness of fracture aperture can be written as follows:

$$\boldsymbol{w_a} = (\boldsymbol{u}^{\boldsymbol{R}} - \boldsymbol{u}^{\boldsymbol{L}}) \cdot \boldsymbol{n}^{\boldsymbol{L}} = -[\boldsymbol{u}] \cdot \boldsymbol{n}^{\boldsymbol{L}} \tag{21}$$

In the following derivation, we simply replace w_a with $\boldsymbol{w_a} = [\boldsymbol{u}^{\boldsymbol{R}} - \boldsymbol{u}^{\boldsymbol{L}}] \cdot \boldsymbol{n}^{\boldsymbol{L}}$. By multiplying the test functions of $\boldsymbol{\delta u}$ and $\boldsymbol{\delta p}$ to Eq. (1), and performing the integration by parts, regrouping the interior faces into paired DG interface sets, and applying the traction boundary conditions, and adopting the jump and average notations defined in Eqs. (19) and (20), we now make a mathematical statement of the IIPG weak formulation for hydraulic fracturing problems as follows:

Find $\boldsymbol{u} \in \mathcal{U}$ and $\boldsymbol{p} \in \mathcal{P}$, and $\boldsymbol{w_a} \in \mathcal{U}$ such that:

$$
\begin{cases}
\mathcal{R}^{u}(\boldsymbol{u},\boldsymbol{p},\delta\boldsymbol{u}) = \int_{\Omega/\Omega_a} \boldsymbol{\sigma}''(\boldsymbol{u}) : \nabla(\delta\boldsymbol{u}) d\boldsymbol{v} \\
\qquad - \int_{\Omega/\Omega_a} \boldsymbol{\alpha} \boldsymbol{p} \nabla \cdot \delta\boldsymbol{u} d\boldsymbol{v} \\
\qquad + \int_{\Omega/\Omega_a} \boldsymbol{f} \cdot \delta\boldsymbol{u} d\boldsymbol{v} \\
\qquad - \int_{S_I} \{\boldsymbol{\sigma}'' \boldsymbol{n}^L\} \cdot [\delta\boldsymbol{u}] d\boldsymbol{s} \\
\qquad + \boldsymbol{\beta} \delta_{pu} \frac{G}{\sqrt{A}} \int_{S_I} [\boldsymbol{u}] \cdot [\delta\boldsymbol{u}] d\boldsymbol{s} \\
\qquad - \int_{\Gamma^{t/a}} \bar{\boldsymbol{t}} \cdot \delta\boldsymbol{u} d\boldsymbol{s} \\
\qquad + \int_{\Gamma^a} \boldsymbol{p} \boldsymbol{n} \cdot \delta\boldsymbol{u} d\boldsymbol{s} \qquad \forall \delta\boldsymbol{u} \in \mathcal{U}^{\mathcal{T}}; \\
\mathcal{R}^{p}(\boldsymbol{u},\boldsymbol{p},\delta\boldsymbol{p}) = \int_{\Omega} \boldsymbol{\alpha} \frac{\Delta \epsilon_v}{\Delta t} \delta\boldsymbol{p} d\boldsymbol{v} \\
\qquad + \int_{\Omega} \frac{1}{M} \frac{\Delta \boldsymbol{p}}{\Delta t} \delta\boldsymbol{p} d\boldsymbol{v} \\
\qquad - \int_{\Omega} s_q \delta\boldsymbol{p} d\boldsymbol{v} \\
\qquad - \int_{\Omega/\Omega_a} \boldsymbol{q} \cdot \nabla \delta\boldsymbol{p} d\boldsymbol{v} \\
\qquad + \int_{S_I} \{\boldsymbol{q} \cdot \boldsymbol{n}^L\} [\delta\boldsymbol{p}] d\boldsymbol{s} \\
\qquad + \boldsymbol{\beta} \delta_{pp} \frac{k}{\mu\sqrt{A}} \int_{S_I} [\boldsymbol{p}] \cdot [\delta\boldsymbol{p}] d\boldsymbol{s} \\
\qquad - \int_{\Gamma^q} \bar{\boldsymbol{q}}_q \delta\boldsymbol{p} d\boldsymbol{s} \qquad \forall \delta\boldsymbol{p} \in \mathcal{P}^{\mathcal{T}}; \\
\mathcal{R}^{w_a}(\boldsymbol{w}_a,\boldsymbol{p},\delta\boldsymbol{p}) = \int_{S_a} \frac{\Delta[\boldsymbol{u}^R - \boldsymbol{u}^L] \cdot \boldsymbol{n}^L}{\Delta t} \delta\boldsymbol{p} d\boldsymbol{s} \\
\qquad - \int_{S_a} \boldsymbol{q}_a \cdot \nabla \delta\boldsymbol{p} d\boldsymbol{s} \\
\qquad - \int_{S_a} \boldsymbol{Q}_a \boldsymbol{w}_a \delta\boldsymbol{p} d\boldsymbol{s} \qquad \forall \delta\boldsymbol{p} \in \mathcal{P}^{\mathcal{T}}.
\end{cases}
\tag{22}
$$

where $\boldsymbol{k}$ and $\boldsymbol{\mu}$ are the permeability and the viscosity of fluids, $\boldsymbol{G}$ the shear modulus of the solid, $\boldsymbol{A}$ the area of an interface, $\boldsymbol{\delta_{pu}}$ and $\boldsymbol{\delta_{pp}}$ without units the stabilized parameters for the solid and fluid field equations, respectively, $\boldsymbol{\beta}$ the control key as introduced in [48] for the opening/closing of DG interface, and $\boldsymbol{\Delta}$ the increment change of variables during a time interval $(\boldsymbol{t^n}, \boldsymbol{t^{n+1}})$. In the first residual equation in Eq. (22) for the solid field, a complete IIPG formulation should involve the average on the total stress and the jump on the test function of the displacement as $\int_{S_I} \{\boldsymbol{\sigma} \boldsymbol{n}^L\} \cdot [\delta\boldsymbol{u}] d\boldsymbol{s} = \int_{S_I} \{(\boldsymbol{\sigma}'' - \boldsymbol{\alpha} \boldsymbol{p} \boldsymbol{I}) \boldsymbol{n}^L\} \cdot [\delta\boldsymbol{u}] d\boldsymbol{s}$. This would result in the coupling of the solid and the fluid fields on interior DG interfaces. However, we observed that such a coupling term does not appear in the second residual equation in Eq. (22) for the pore pressure equation. To be consistent to the coupling of two fields contributed from the volume integration, we simply drop this two-field coupling effect on DG interfaces. It should be understood

that the term of $\int_{\Gamma^a} \boldsymbol{pn}\cdot\boldsymbol{\delta u}\boldsymbol{ds}$ in the first residual equation in Eq. (22) is the implicit pressure loading induced from injected fluids in apertures as it is a part of solution.

We now discuss the opening of DG interfaces for crack propagation. In this DG formulation, we assume that all actual crack paths are along the predefined DG interfaces and all fluid flow elements in fracture apertures are also predefined and completely constructed as middle surfaces using DG interfaces. The construction of such middle surface elements for aperture fluid flow will be demonstrated in later section. Before cracks open, parameter $\boldsymbol{\beta}$ is set to $\mathbf{1}$ for each quadrature point on the DG interface. In this case, a continuous bulk solid field and a continuous bulk fluid field across DG interfaces are modeled by enforcing constitutive laws for bulk solids and bulk fluids. The third equation in Eq. (22) is also inactive. If the failure criterion of any quadrature point on DG interfaces is satisfied, the traction will be gradually released through making the cohesive model active and also putting $\boldsymbol{\beta} = \mathbf{0}$. For this case, the third equation in Eq. (22) will be active. Specifically, due to the activation of cohesive models on opening DG interfaces, the first equation in Eq. (22) for the solid field can be more precisely rewritten as follows:

$$\begin{aligned}\mathcal{R}^{\boldsymbol{u}}(\boldsymbol{u},\boldsymbol{p},\boldsymbol{\delta u}) = \quad & \int_{\Omega/\Omega_a} \boldsymbol{\sigma}''(\boldsymbol{u}) : \nabla(\boldsymbol{\delta u})\boldsymbol{dv} - \int_{\Omega/\Omega_a} \boldsymbol{\alpha p}\nabla\cdot\boldsymbol{\delta u}\boldsymbol{dv} \\ & + \int_{\Omega/\Omega_a} \boldsymbol{f}\cdot\boldsymbol{\delta u}\boldsymbol{dv} - \int_{S_I} \boldsymbol{T}([\boldsymbol{u}])\cdot[\boldsymbol{\delta u}]\boldsymbol{ds} \\ & - \int_{\Gamma^{t/a}} \bar{\boldsymbol{t}}\cdot\boldsymbol{\delta u}\boldsymbol{ds} + \int_{\Gamma^a} \boldsymbol{pn}\cdot\boldsymbol{\delta u}\boldsymbol{ds}\end{aligned} \tag{23}$$

where $\boldsymbol{T}$, the traction the DG interface, is a function of the jump of displacement across the interface prescribed by cohesive laws. $\boldsymbol{T}$ can be further written in terms of DG notations as follows:

$$\boldsymbol{T}([\boldsymbol{u}]) = \frac{\mathbf{1}}{\mathbf{2}}\left((\boldsymbol{T}_n^L([\boldsymbol{u}]) + \boldsymbol{T}_n^R([\boldsymbol{u}]))\boldsymbol{n}^L + (\boldsymbol{T}_t^L([\boldsymbol{u}]) + \boldsymbol{T}_t^R([\boldsymbol{u}]))\boldsymbol{t}^L\right). \tag{24}$$

where notations $\boldsymbol{T}_n$ and $\boldsymbol{T}_t$ are the normal and tangent components of the traction on the crack surface. These traction components are functions of $[\boldsymbol{u}]$, which are defined in the cohesive model in Eq. (12). The notation $\boldsymbol{t}^L$ in Eq. (24) is the tangent vector from the left side surface for a DG interface and can be further calculated as follows:

$$\boldsymbol{t}^L = \frac{\boldsymbol{T}^L - \boldsymbol{T}_n\boldsymbol{n}^L}{|\boldsymbol{T}^L - \boldsymbol{T}_n\boldsymbol{n}^L|}. \tag{25}$$

Remark I. Rigid cohesive laws are more physical models as they avoid initial artificial stiffnesses required for conventional cohesive models. However, due to the infinity in initial stiffness, it is very hard to implement rigid cohesive laws into CZM finite element frameworks unless some ad hoc methods are applied. We argue that rigid cohesive laws can be elegantly implemented in DG frameworks. As shown in the first equation in Eq. (22), before DG interfaces fail, the stiffness of DG interfaces are computed using normal elastic moduli of bulk solids. When materials on interfaces start to fail, the softening stiffness of cohesive models is computed. Therefore, rigid cohesive models incorporated in DG formulations never involve the numerical issue on computing the infinity for initial stiffness. More precisely, with regard to hydraulic fracturing, such an elegant incorporation of rigid cohesive laws in DG formulations results in a clean and accurate calculation on stresses around crack tips for the solid field, which also benefit to have a clean and accurate calculation on both pore pressure in bulk matrices and fluid pressure in apertures. Consequently, the convergence in terms of the Newton iterations for implicit methods may be much improved.

We now address some options in making fluid flow active in the apertures newly formulated from crack openings. The aperture flow is activated once: (1) tractions in all quadrature points in a cracked surface are completely released; (2) materials in all quadrature points in a cracked surface start to fail (softening). In this work, any quadrature point in a cracked surface starts to fail (softening), the aperture flow at that quadrature point will be activated. It should be mentioned that optional one is too conservative and should not be used as its predicted COD tends to be smaller.

Finally, we discuss the choices for the stabilized parameters in our IIPG formulation. A wide and continuous range of IIPG stabilization parameters has been observed in [42,44,57] for solving nearly incompressible elasticity, finite plasticity, and poromechanics problems. $[\mathbf{1}, \mathbf{10^5}]$ may be a suitable range for both $\delta_{\mathbf{pu}}$ and $\delta_{\mathbf{pp}}$ for poromechanics problems solved using IIPG methods. $\delta_{\mathbf{pu}} = \mathbf{10}$ and $\delta_{\mathbf{pp}} = \mathbf{10}$ are used for all runs in this work.

3.2. Linearization

The nonlinearity of Eq. (22) is attributed from: (a) the potential large deformation of the solid phase that may include large openings of crack surfaces; (b) the pressure loading acting on aperture wall surfaces, i.e. a follower load that may greatly impact on nonlinear iteration procedures through contributing the algebraic tangent modulus in solvers; (c) the softening cohesive laws for crack openings, which will be adopted in this work; and (d) the nonlinear constitutive law (the cubic lubricating theory) for the flow in apertures. A robust implicit DG formulation for hydraulic fracturing problem in porous media must be derived by consistently linearizing these nonlinear sources in Eq. (22). Here, we assume that all material model parameters such as the elastic material parameters, the porosity, Biot's coefficient and modulus, and fluid model parameters such as viscosity are assumed to be constant during injection. To perform the linearization on these coupled and complex residuals in Eq. (22), we adopt a so called a material time derivative method that has been adopted in [44,51] to linearize purely solid mechanics problems undergoing finite hyperelastoplasticity deformation and coupled solid and fluid flow porous medium problems in large plastic deformation. Since the derivation of the linearization on coupled three-field equations are technically intensive, we present such a derivation in Appendix. Following the linearization in the Appendix, the linearized system for the coupled solid, bulk fluid flow, and aperture flow hydraulic fracture problem can be written in a form of symbolic algebraic equations as follows:

$$\begin{bmatrix} \boldsymbol{K}^{uu} & \boldsymbol{K}^{up_b} & \boldsymbol{K}^{up_a} \\ \boldsymbol{K}^{p_{bu}} & \boldsymbol{K}^{p_bp_b} & \boldsymbol{K}^{p_bp_a} \\ \boldsymbol{K}^{p_au} & \boldsymbol{K}^{p_ap_b} & \boldsymbol{K}^{p_ap_a} \end{bmatrix} \begin{bmatrix} \delta\boldsymbol{u} \\ \delta\boldsymbol{p}_b \\ \delta\boldsymbol{p}_a \end{bmatrix} = \begin{bmatrix} \boldsymbol{R}^u \\ \boldsymbol{R}^p \\ \boldsymbol{R}^{w_a} \end{bmatrix} \tag{26}$$

where $\boldsymbol{u}$, $\boldsymbol{p}_b$, and $\boldsymbol{p}_a$ are primary unknowns in solutions for the displacement of the solid field, the pore pressure of the bulk fluid, and the fluid pressure of the aperture.

4. Implementation

4.1. Co-rotational framework

For hydraulic fracturing problems, fracture apertures may often undergo large openings, which requires numerical methods implemented in finite deformation frameworks. In this work, we implement our DG formulation in co-rotational framework in the hypo-elasticity framework. The co-rotational formulation is to satisfy the principle of material frame-indifference through implementing material laws in a rotated configuration based on the decomposition of the deformation gradient. The deformation gradient $\boldsymbol{F}$ is defined as the derivative of the mapping function $\boldsymbol{\phi}$ with respect to the reference coordinate X as follows:

$\boldsymbol{F}(\boldsymbol{X}, \boldsymbol{t})$ can be multiplicatively decomposed into a rotational tensor $\boldsymbol{R}(\boldsymbol{X})$ and a stretch tensor $\boldsymbol{U}(\boldsymbol{X})$ as follows:

$$\boldsymbol{F}(\boldsymbol{X}, \boldsymbol{t}) = \boldsymbol{R}(\boldsymbol{X}, \boldsymbol{t})\boldsymbol{U}(\boldsymbol{X}, \boldsymbol{t}). \tag{27}$$

To apply material hypoelastic constitutive laws, the objective stress $\boldsymbol{\sigma}^{\boldsymbol{o}}$ in an incremental or rate form within the co-rotational formulation is defined as follows:

$$\boldsymbol{\sigma}^{\boldsymbol{o}} = \boldsymbol{R}\dot{\boldsymbol{\sigma}}'\boldsymbol{R}^T \tag{28}$$

where $\dot{\boldsymbol{\sigma}}'$ is the rate form of the Cauchy stress in the rotated domain and the rotated Cauchy stress $\boldsymbol{\sigma}'$ can be updated in the rotated domain as discussed below. The procedures of the co-rotational formulation for the solid field are summarized as follows [44,55]:

$$\begin{cases} \Delta\boldsymbol{\epsilon}' = \boldsymbol{R}^T\Delta\boldsymbol{\epsilon}\boldsymbol{R}; \\ \boldsymbol{\epsilon}' = \boldsymbol{\epsilon}'_n + \Delta\boldsymbol{\epsilon}'; \\ \boldsymbol{\sigma}' = \boldsymbol{C}'\boldsymbol{\epsilon}'; \\ \boldsymbol{\sigma} = \boldsymbol{R}\boldsymbol{\sigma}'\boldsymbol{R}^T \\ \boldsymbol{C}_{ijkl} = \boldsymbol{T}_{im}\boldsymbol{T}_{jn}\boldsymbol{T}_{kp}\boldsymbol{T}_{lq}\boldsymbol{C}'_{mnpq} \end{cases} \tag{29}$$

where $\boldsymbol{C}'$ is the material elasticity tensor defined in the rotated domain, $\boldsymbol{\epsilon}'$, $\boldsymbol{\epsilon}'_n$, $\Delta\boldsymbol{\epsilon}'$, and $\boldsymbol{\sigma}'$ the current total elastic strain, the total elastic strain at the previous time step, the incremental elastic strain, and the total Cauchy stress in

the co-rotational configuration, respectively, and $\boldsymbol{\Delta\epsilon}$, σ, $\boldsymbol{C}$ the incremental elastic strain, total Cauchy stress and material elasticity tensor in the current domain, respectively. It should be mentioned that a successful implementation of the co-rotational formulation is on a robust algorithmic construction of the rotational tensor $\mathbf{R}$ in Eq. (27). For the detailed formation of the rotational tensor $\mathbf{R}$ and a robust algorithm to numerically perform the decomposition of deformation gradient $\mathbf{F}$, we refer to [55,56].

4.2. Transformation of local permeability tensor

For general apertures in three dimensions, their fracture permeability (or conductivity) tensors are locally defined as Eq. (11). More precisely, even though the permeability of a porous medium is isotropic, the fracture permeability is globally non-isotropic due to the change in the direction of fracture propagation. To be objective, the local fracture permeability must be transformed into the global system for the assemble of elements. The transformation matrix T is a function of the normal directional vector n of the middle surface of an aperture and the transformation is carried out as follows:

$$\mathcal{D}^{a^G} = \boldsymbol{T}^T(\boldsymbol{n})\mathcal{D}^a\boldsymbol{T}(\boldsymbol{n}) \tag{30}$$

where $\mathcal{D}^{a^G}$ is the global fracture permeability/conductivity tensor.

4.3. Enhancement of DG data structures for fracture surface integration

The calculation of the tangent stiffness and residual vector based on the fracture flow equation involves the integration of variables on a general 3D surface. Compared with the dominated volume-integration method within CG formulations, a 3D surface integration requires some additional effort on dealing with surface orientations. In our previous DG code implementations [44,46,52,57], a nodal-based DG framework has been well developed by grouping continuous elements into a few element sets. In this paper, all presented numerical problems are solved using 3D hexahedral elements as well as 3D DG interface elements. For an easy presentation of DG ideas, first, we illustrate the construction of DG interfaces using 2D mesh shown in Fig. 4(a)–(c). As illustrated in Fig. 4(a)–(c), some continuous elements on a potential crack path are highlighted and grouped into two sets, the left side and the right side. After setting up these two set elements, an element breaking subroutine in our DG code is called to general DG interfaces shared by the left and right elements through adding some additional nodes to the CG mesh. First, we underline that from the user point of view, the operation of highlighting and grouping elements is much easier than inserting elements, e.g. CZM elements into a continuous mesh. Second, in our nodal-based DG code, an interface is always defined as a surface of an element and its normal vector is always outward to the element. This is not the case for the middle surface of a fracture aperture. More precisely, our interface variable integration is finished by simply inserting the natural coordinates of the Gaussian integration points on the element surfaces. Finally, Fig. 4(d) further illustrates the construction of a 3D middle surface element for fluid flow in apertures using the existing paired DG interfaces. In Fig. 4(d), we duplicate the left side element of the aperture and replace the nodes of this duplicated element on the aperture wall using the middle surface pressure nodes that are pre-assigned for fractures by referring the corresponding opened DG interfaces. Consequently, by associating the middle surface of a fracture aperture with an surface of an DG element, the variable integration on a fracture flow surface can be nicely carried out by calling all existing DG routines, e.g.:

$$\int_{S_a} \boldsymbol{D}^a\nabla\dot{\boldsymbol{p}}\cdot\nabla(\delta\boldsymbol{p})\boldsymbol{ds} \Longrightarrow \int_{S_I(\chi)} \boldsymbol{D}^a\nabla\dot{\boldsymbol{p}}\cdot\nabla(\delta\boldsymbol{p})\boldsymbol{ds} \tag{31}$$

where $\boldsymbol{\chi}$ is the DG element set.

5. Benchmark and application

In this section, first, we verify our DG formulation and implementation by solving a plane strain KGD benchmark problem that involves a single symmetric crack propagation in an infinite elastic porous media. We compare our DG predictions with the analytical solutions of this benchmark including the displacement opening at the injection point, the distance of the fracture propagation, and the diffuse of the fluid pressure at the injection point. With the confidence in the good performance of our DG methods in solving this benchmark, we further test our DG

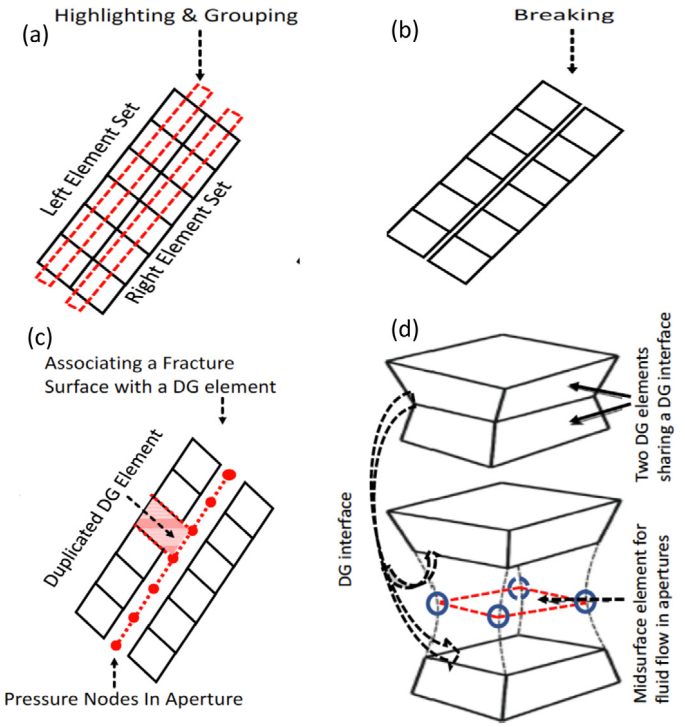

Fig. 4. Enhancement of DG interface data structures for fracture openings and fluid flow in apertures: an illustration of highlighting and grouping continuous elements in (a), breaking CG element sets in (b), associating a DG interface with a crack surface in (c), constructing 3D middle surface elements for fluid flow in apertures using DG elements in (d).

framework by solving a more complex and interesting hydraulic fracturing problem that involves two nature fracture propagation in an oil reservoir.

5.1. KGD benchmark

Fig. 5(a) illustrates the profile of a **60** m × **45** m plane strain KGD model. In this model, for the solid field, the displacements in the x-direction at the left and right sides and the displacement in the y-direction at the bottom of the block are constrained as indicated by rollers in the figure. The red lines in Fig. 5(a) indicate the no flow boundary conditions for the fluid flow field. The initial stresses and initial pore pressure are assumed to be zero for the whole domain. A fluid is injected at a flow rate of $\boldsymbol{Q_a/2 = 0.0005}$ m^3/s at the middle point in the bottom of the block. Linear and isotropic elasticity is assumed for the solid field. Model material parameters including the Young's modulus ($\boldsymbol{E}$), Poisson's ratio ($\boldsymbol{\nu}$), Biot's coefficient ($\boldsymbol{\alpha}$), Biot's modulus ($\boldsymbol{M}$), permeability ($\boldsymbol{k}$), and viscosity ($\boldsymbol{\mu}$) of the injection fluid are listed in Table 1. The model parameters of a rigid linear softening cohesive law are also listed in Table 1.

It should be noted that as the cohesive energy $\boldsymbol{G_c}$ is listed in Table 1, the fracture toughness parameter $\boldsymbol{K_{Ic}}$ is redundant. As the closed solutions discussed below from references for the toughness storage case are written in terms of $\boldsymbol{K_{Ic}}$, we also include it in Table 1 for convenience. The closed solutions for this benchmark are available within an asymptotic framework. These solutions depend on the energy dissipation mechanisms in terms of either fracture extension or fluid viscous flow in fractured channels. The storage of injected fluids includes the leak-off of fluids into porous solid bulk matrix or fluid accumulated in propagated apertures. Four different analytical solutions corresponding to storage-toughness, storage-viscosity, leak-off-toughness, and leak-off-viscosity model cases have been derived in [5,6,8,11]. In this work, we focus the storage-toughness case. The storage-toughness model is placed by simply setting a very low value of viscosity for the injected fluid. To compare with the prediction from

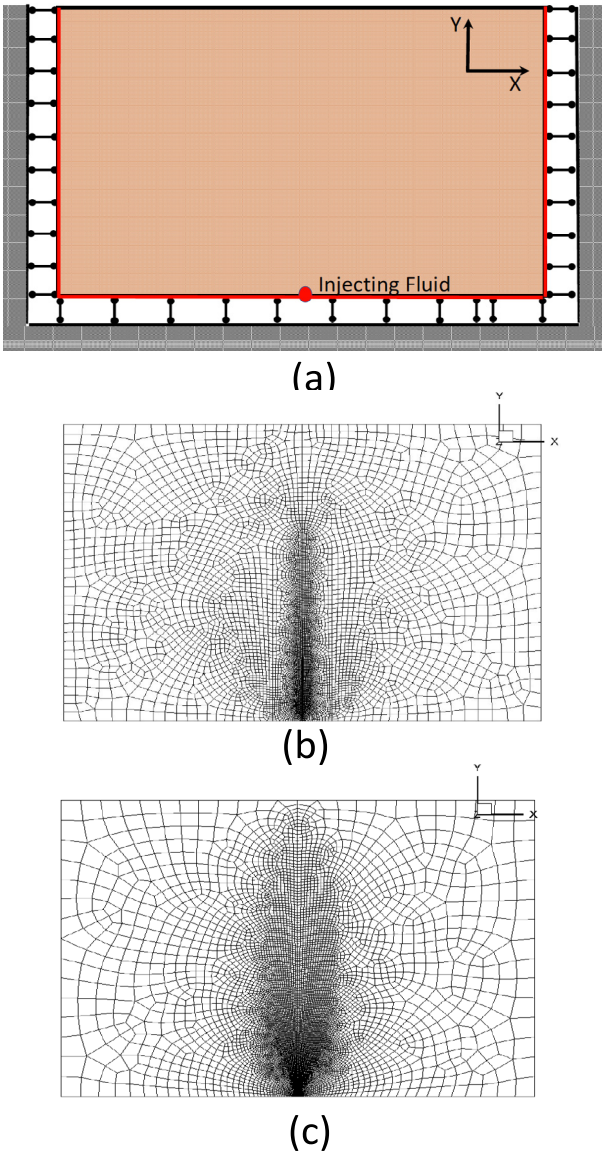

Fig. 5. KGD finite element model: (a) Illustration of plane strain KGD model and boundary conditions; (b) Mesh I with 7500 elements and 200 DG interfaces along crack path; (c) Mesh II with 10 000 elements and 300 DG interfaces along crack path.

our proposed DG method, we summarize the closed solutions for this benchmark problem derived in [6], as follows:

$$\begin{cases} \boldsymbol{w}(\boldsymbol{0},\boldsymbol{t}) = \boldsymbol{\pi}^{-\frac{1}{3}}(\frac{\boldsymbol{K}'}{\boldsymbol{E}'})^{\frac{2}{3}}\boldsymbol{Q}_a{}^{\frac{1}{3}}; \\ \boldsymbol{l}(\boldsymbol{0},\boldsymbol{t}) = (\frac{\boldsymbol{E}'\boldsymbol{Q}_a}{\boldsymbol{K}'})^{\frac{2}{3}}\boldsymbol{t}^{\frac{2}{3}}\frac{\boldsymbol{2}}{\boldsymbol{\pi}^{\frac{2}{3}}}; \\ \boldsymbol{p}(\boldsymbol{0},\boldsymbol{t}) = (\frac{\boldsymbol{K}'^{4}}{\boldsymbol{E}'^{4}\boldsymbol{Q}_a\boldsymbol{t}})^{\frac{1}{3}}\boldsymbol{E}'\frac{\boldsymbol{2}^{-3}}{\boldsymbol{\pi}^{-\frac{1}{3}}}, \end{cases} \tag{32}$$

where $\boldsymbol{w}(\boldsymbol{0},\boldsymbol{t})$, $\boldsymbol{l}(\boldsymbol{0},\boldsymbol{t})$, and $\boldsymbol{p}(\boldsymbol{0},\boldsymbol{t})$ are the crack opening displacement (COD) at the injection point, the length of fracture extension measured from the injection point, and the injection pressure developed in the injection point.

Table 1
KGD model parameters.

Parameters	Value
Young's modulus	$E = 17$ GPa
Poisson's ratio	$\nu = 0.2$
Biot's coefficient	$\alpha = 0.75$
Biot's modulus	$M = 68.7$ MPa
Permeability	$k = 0.1$ mD
Fluid viscosity	$\mu = 0.1$ cP
Cohesive energy	$G_c = 120$ Pa m
Cohesive strength	$T_0 = 1.25$ MPa
Fracture toughness	$K_{Ic} = 1.46$ MPa $\sqrt{\text{m}}$
Mode control	$\gamma = 0$
Injection rate	$Q_a = 0.001$ m^3/s

In Eq. (32), parameters $\boldsymbol{E'}$ and $\boldsymbol{K'}$ are further computed as $\boldsymbol{E'} = \frac{\boldsymbol{E}}{\boldsymbol{1-\nu^2}}$ and $\boldsymbol{K'} = (\boldsymbol{4}(\frac{\boldsymbol{2}}{\boldsymbol{\pi}})^{\frac{\boldsymbol{1}}{\boldsymbol{2}}})\boldsymbol{K_{IC}}$ where $\boldsymbol{K_{IC}}$ is the mode-I fracture toughness.

First, to solve this KGD model using the proposed IIPG method, Fig. 5(b) presents a finite element mesh projected in xy plane. It should be mentioned that total one layer 7500 three-dimensional continuous hexahedral elements along the Z-direction are meshed. To solve an equivalent plane strain KGD model, we enforce the condition of zero-displacement along the Z-direction for all nodes in the mesh. More than 90% of elements are placed within a narrow band in the middle of the body on which the fracture will occur. As the fracture path is known to be on the middle of the body, we simply group a total of continuous 400 elements along the middle and break these continuous elements into DG elements. Total DG elements are only 5% of total elements. By breaking these 400 CG elements, a total of 200 DG interfaces are placed on the potential crack path to accommodate the event of crack openings. These 200 DG interfaces are initialized to the unreleased or unopened state. Second, to trig the extension of fractures, a released or opened state for the first DG interface located in the injection point is technically enforced. The opening aperture of this interface is initialized by 0.01 mm. As this special interface is set to a complete opened state, the enforcement of the cohesive law for interface traction release and the assembling of the stiffness and force for this DG interface with regard to the solid field are all bypassed. Furthermore, the flow in this opened interface is activated and the fluid pressure in this opened aperture induced from fluid injection is applied on the aperture surface to enforce the coupling condition of fracture flow and solid deformation. Finally, our simulation was carried out by 20 s and total 8000 time steps are applied. With regard to nonlinear iterations in solving this problem, we observe that solutions converge within **2** or **3** iterations in each time step.

We now discuss simulation results from our IIPG method. Fig. 6(a) and (b) present the final profiles of fracture propagation for the storage-toughness model. In these figures, our DG framework predicts the final values for COD, fracture length, and fluid pressure that are measured at or from the injecting point are **0.78** mm, **16.1** m, and **0.29** MPa, respectively. Fig. 6(a) shows the contour of the injecting pressure gained at $\boldsymbol{t} = \boldsymbol{20}$ s and From Fig. 6(a), we observe that a negative pressure appears near the front of the crack tip. This implies that our DG formulation correctly predicts this small negative pore pressure area in the front of the fracture tip. One reason for having such a negative pressure contour is that in this KGD model, the initial pore pressures in the bulk matrix are zeros. Another reason is that the fracture tip front in the solid skeleton is in a tension state resulting from an external pressure loading exerted from injected fluids in the fracture. Consequently, this implies that the fluid in the bulk matrix (not fluid stored in fractures) around the fracture front flows into the front region of the fracture tip. Fig. 6(b) plots the stress in x-direction predicted over the whole domain at $\boldsymbol{t} = \boldsymbol{20}$ s. Again, the predicted lobe shape of the normal stress in the x-direction around the crack tip is consistent to the typical tip stress profiles described in the conventional linear fracture mechanics for pure solid phase problems.

Fig. 7(a)–(c) plot the IIPG predictions (red solid lines) on the COD, the distance of fracture extension, and the aperture pressure following the injecting time for the storage-toughness KGD model, respectively. All these predictions are measured at the fracture mouths/injecting nodes. For comparison, the corresponding closed solutions obtained from Eq. (32) are also plotted in Fig. 7. Fig. 7(a) and (b) display a fast increase in the COD grow at the early injecting time and a slow increase in the COD development after a few second of injection. By evaluating

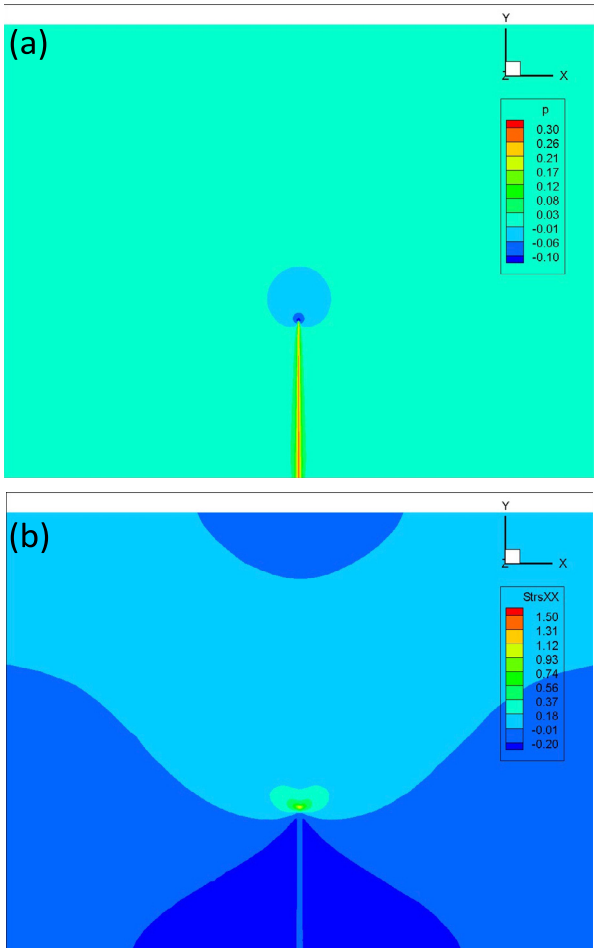

Fig. 6. Contours of IIPG predictions on (a) pressure at injecting point and (b) normal stress in the x-direction at t = 20 s.

Fig. 7(a) and (b), we conclude that the predictions of our DG framework on both the COD and the length of fracture propagation agree well with those obtained from the closed solutions for this storage-toughness model.

In Fig. 7(c), our DG framework predictions show higher pressure values developed on the injecting points than those obtained from the corresponding analytical pressure. These higher predictions on pressures have been also reported in [29,30,32] where CZM or XFEM methods are adopted. As further discussed in [29], the predictions from numerical methods are always greater than the pressure obtained analytically. This is because the coupled effect of the solid and flow is neglected in the analytical models and the increase in the pore pressure of the surrounding porous bulk matrix in the coupled solid and fluid flow in the adopted numerical methods that induces the back stresses [58] that in turn generate an additional compressive stress. The COD and the length of fracture propagation are not affected by the increased injecting pressure in fracture apertures due to the poroelastic effect [59].

Finally, to study the impact of mesh topology on the predictions we design a new mesh having total 10,000 elements, total 300 DG interfaces on a length of 20 m crack path, and a wider fine zone around the crack. The topology of this new mesh is shown in Fig. 5(c). Its predictions are plotted in dashed red lines in Fig. 7(a)–(c). Furthermore, Fig. 7(a) and (c) also present some CZM predictions on the COD and the injection pressure (red solid dots) from reference [30] having similar number of elements near the crack path to our mesh shown in Fig. 5(c). Reference [30] shows that the predicted curves would exhibit a zig-zag behavior until the mesh is fine enough. We conclude that predictions from our two different meshes and reference [30] are very smooth and have no obvious difference (less than 1%).

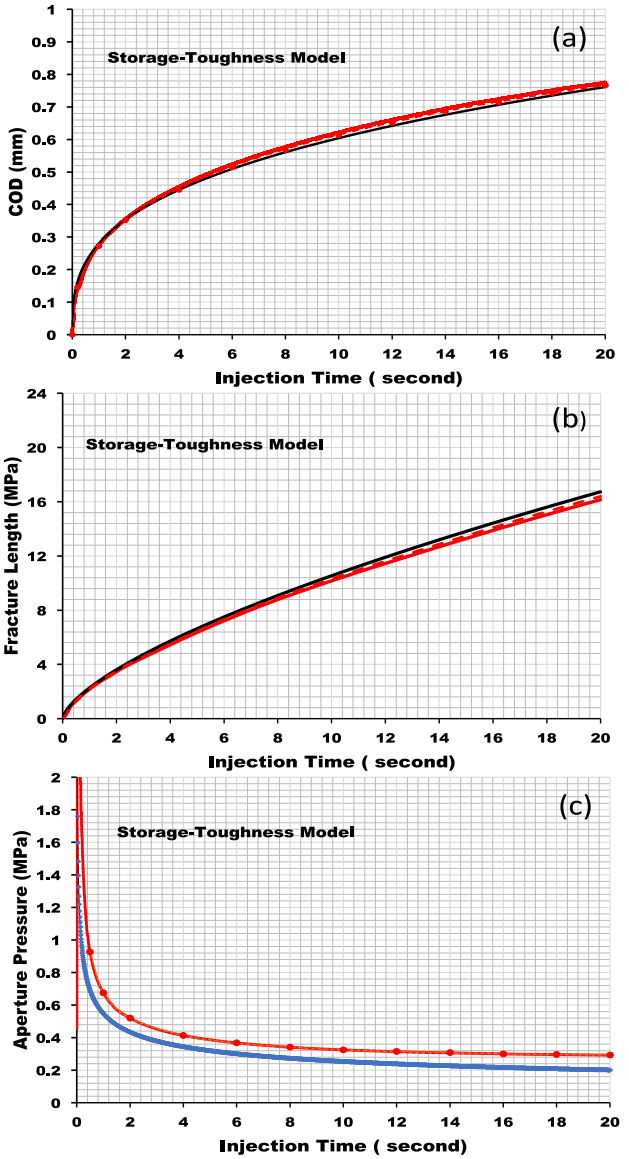

Fig. 7. Comparison between the IIPG predictions, the closed solutions, and the predicted solutions from other numerical methods for KGD model on (a) COD, (b) fracture length, and (c) pressure at injection point. Dark line: closed solutions; Red solid line: prediction from IIPG with relatively coarse mesh; Red dashed line: prediction from IIPG with relatively fine mesh; Red solid circle: prediction from reference [30] where CZM method and relative fine mesh are used. Note: Prediction on fracture length was not reported in reference [30].

5.2. Interaction of two natural fractures in reservoirs

The fracture in the KGD model solved above is symmetric and always propagates along the vertical direction. To further test the capability of our proposed DG formulation and implementation for solving hydraulic fracturing problems, we solve a more complex hydraulic fracturing problem that contains two large and isolated fractures initially filled with reservoir fluids. We investigate the interaction between these two natural fractures by injecting fluid in one fracture. Fig. 8 shows that a porous medium block contains a stiff and nearly impermeable overburden and an under-burden with the same dimensions of **100** m $\times$ **32.5** m, and a soft and permeable oil/gas reservoir layer with dimensions of **100** m $\times$ **25** m in the middle of the block, and a large slant aperture explicitly embedded in the middle of the reservoir along **26.3** degrees with respect to the horizontal direction and a relatively short aperture

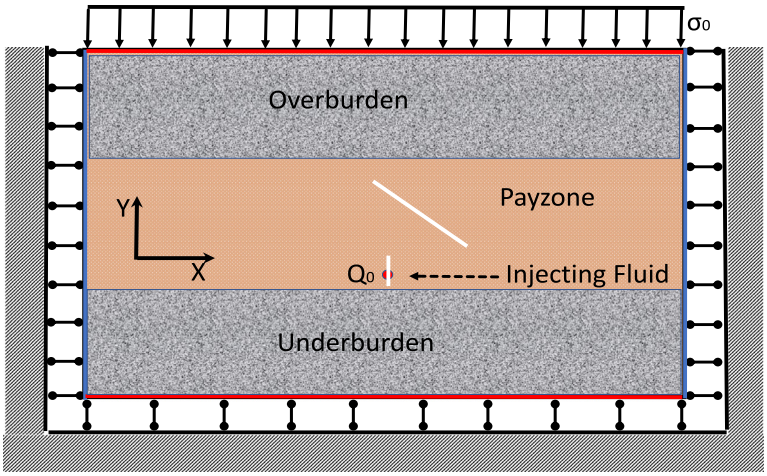

Fig. 8. Illustration of a two natural fracture model and its boundary conditions.

Table 2
Two natural fracture model parameters.

Parameters	Value
Young's modulus (Overburden and underburden)	E = 50 GPa
Young's modulus (Payzone)	E = 10 GPa
Poisson's ratio	$\nu = 0.2$
Biot's coefficient	$\alpha = 1.0$
Biot's modulus	M = 68.7 MPa
Permeability (Overburden and Underburden)	k = 0.001 mD
Permeability (Payzone)	k = 0.1 mD
Fluid viscosity	$\mu_f = 1$ cP
Cohesive energy	$G_c = 360$ Pa m
Cohesive strength	$T_0 = 3.5$ MPa
Fracture toughness	$K_{Ic} = 1.37$ MPa $\sqrt{\text{m}}$
Mode control	$\gamma = 0$
Injection rate	$Q_a = 0.005$ m^3/s

embedded in the middle and along the vertical direction. The lengths of the larger and the smaller fractures are 13 m and **2.6** m, respectively. Displacements in the left and right sides of the model are constrained in the horizontal direction (x) and the bottom of the block is constrained in the vertical direction (y). All displacements in the z-direction are constrained to enforce the plane strain condition for the problem. An overburden pressure up to **30** MPa is applied on the top surface on the overburden. For the flow field, the pore pressures in the left and right sides are enforced by **20** MPa. An initial pore pressure of **20** MPa is placed for the whole domains including the overburden, under-burden, and the reservoir layer. An initial thickness for these two fracture apertures is set by **4** mm. The aperture shrinks by roughly **2** mm after the overburden is loaded and the stress balance is attained by initiation. We inject fluids into the short fracture and predict how these two fractures propagate. Solid material parameters, fluid properties, and fracture model data, and fluid injection rate are listed in Table 2.

Comparing with the KGD model, a significant complexity gained in this two natural fracture model includes: (a) The determination of the initial stress state that preserves the stress balance in the whole model. This initialization is performed by running the whole coupled model for **5** time steps and by proportionally applying the overburden pressure and reservoir pressure up to the required level. While the solid is assumed to be elastic, it is necessary to run multiple time steps at this initiation stage as the whole model is solved in the sense of large deformation taking into the effect of geometrical nonlinearity; (b) The placement of the predefined DG interfaces along potential crack paths. Unlike the KGD model where crack direction is known in advance, the directions of fracture propagation are

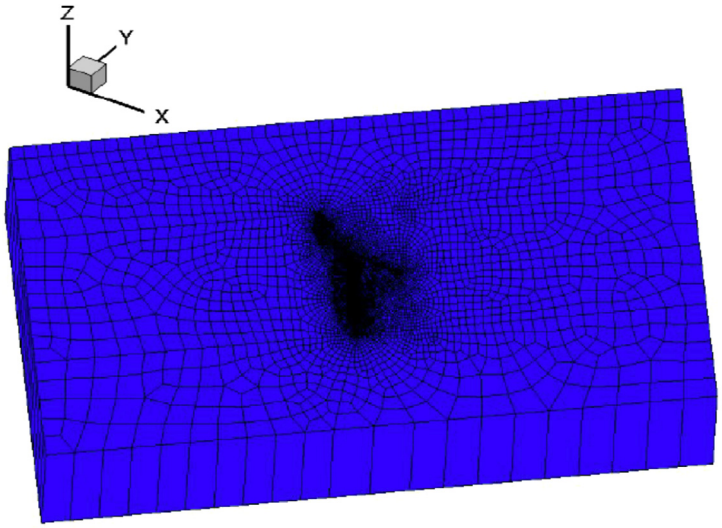

Fig. 9. Final adaptive mesh with 3D hexahedral elements for two natural fracture model.

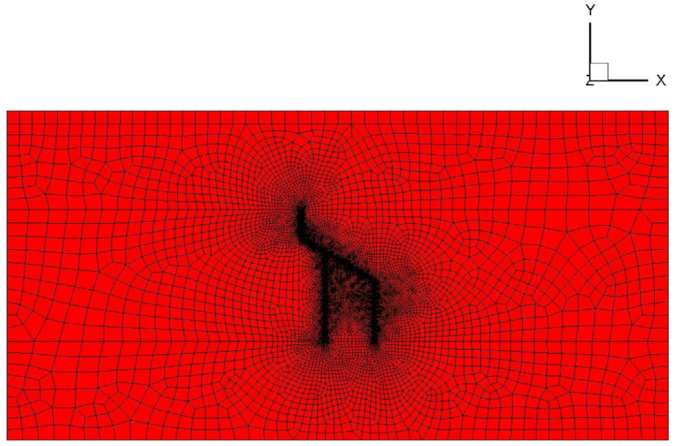

Fig. 10. Final adaptive mesh projected on xy-plane for two natural fracture model.

unknown for this two crack model. To solve this challenge, we adopt the trial-error method that has been used to successfully solve a more than **20** hydride crack problem in [52]. Basically, after a quick investigation, we exclude the possibility of crack paths along, toward, or across the horizontal direction as the larger effective stress in the vertical direction would prevent any fracture from propagating along the horizontal or across the horizontal direction. After a few job runs, by evaluating the effective stress components and the von Mises stress we conclude that the smaller fracture most likely propagates along its initial vertical direction and the larger crack would most likely turn sharply to propagate toward the vertical direction after the smaller fracture propagates and meets the larger fracture. It should be noted that meshes have effects on crack paths. For spatial convergence of crack nucleation and removing mesh bias in modeling cracks we refer. Fig. 9 shows the final 3D hexahedral mesh for solving this two natural fracture problem. Again, a single layer element along the z-direction is attained in the whole domain. we solve this plane strain model by making displacement constrained in the z-direction. For meshing, we maintain a similar size to that of the KDG benchmark solved in the previous section. In the model, total **27**, **000** hexahedral elements are meshed and total **600** DG interfaces are constructed around the two apertures and potential fracture paths. Fig. 10 shows a more detailed 2D topology view in the xy-plane; (c) The careful setup of the data structure for fluid flow at the intersection at which two fractures meet together; (d) The complex pressure build-up and dropping

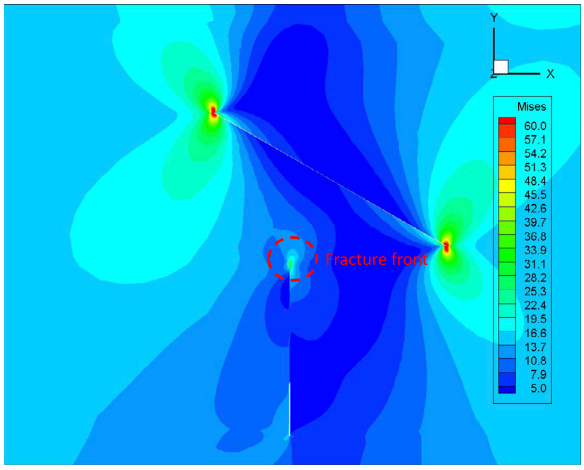

Fig. 11. Fracture extension of the smaller crack to its halfway toward the larger aperture. Injection time: t = 1.98 s.

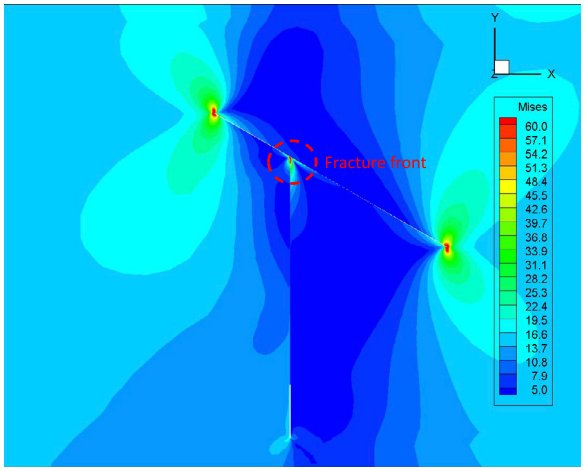

Fig. 12. The smaller crack finally reaches the larger aperture but they are not connected yet. Injection time: t = 3.42 s.

down behavior resulting from multiple physical events including the smaller crack propagation, coalescence of two fractures, and the larger crack propagation; and finally, (f) An unexpected fracture surface contact event. This event will be discussed in detail at the end of this section.

Again, with regard to nonlinear iterations in solving this two fracture problem, we observe that in each time step, solutions converge within **2** or **3** iterations. Fig. 11 plots the von Mises stress on a roughly half of journey for the smaller fracture propagating toward the larger aperture at $\boldsymbol{t = 1.98}$ s. Fig. 12 plots the contour of the von Mises stress just before the smaller fracture connects the larger aperture at $\boldsymbol{t = 3.42}$ s. At $\boldsymbol{t = 3.57}$ s, two fractures eventually connect each other as shown in Fig. 13. Fig. 14 displays the von Mises contour at $\boldsymbol{t = 13.3}$ s. As the pressure build-up slows down due to the coalescence of two fractures, it takes longer time for injection to initiate the propagation of the larger fracture toward to the vertical direction. Fig. 15 shows the stress profile of the fracture initiation for the larger aperture at $\boldsymbol{t = 13.5}$ s. Finally, at $\boldsymbol{t = 15.2}$ s, the whole fracture propagation is arrested at the intersection of the payzone and the overburden as shown in Fig. 16. We plot the variation of the aperture pressure versus the injecting time measured at the injection point in Fig. 17. Fig. 17 shows a much more complex and dynamic behavior of aperture flow for the two-fracture model than the KGD model. In summary, each loop on the increase and decrease in pressure presented in Fig. 17 connects an opening event of interfaces and the stopping of fracture extension.

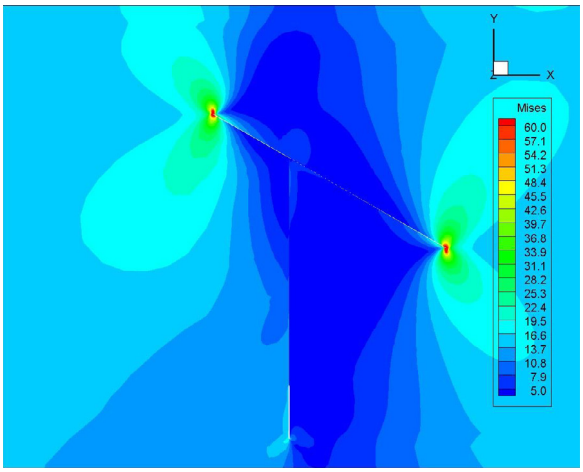

Fig. 13. The two cracks eventually meet. Injection time: t = 3.57 s.

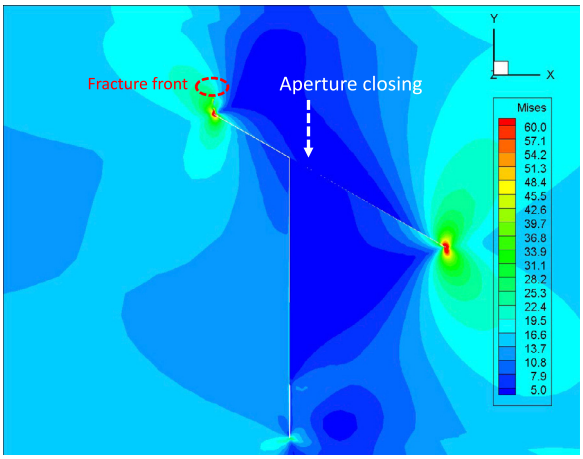

Fig. 14. The larger crack starts to propagate vertically towards the overburden. Injection time: t = 13.3 s.

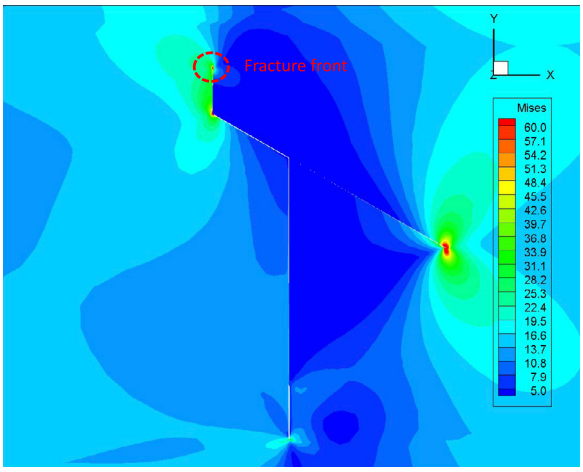

Fig. 15. The larger crack extensively propagates vertically towards the overburden. Injection time: t = 13.5 s.

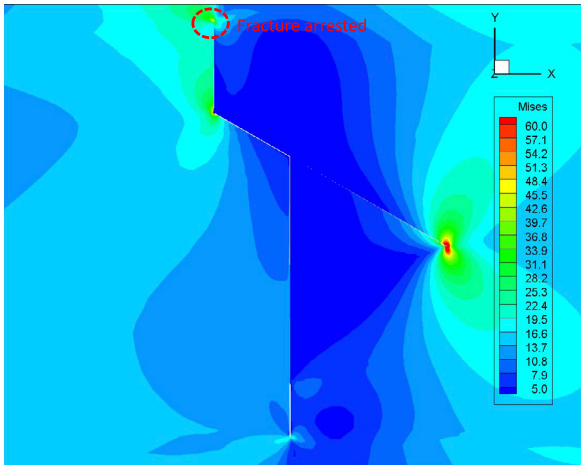

Fig. 16. Finally, the fracture propagation is arrested. Injection time: t = 15.2 s.

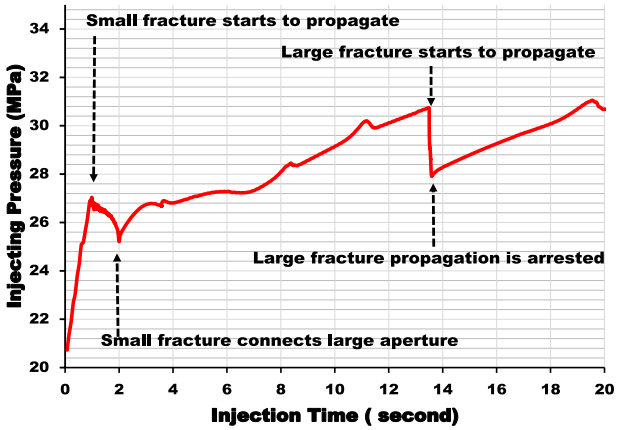

Fig. 17. Injecting pressure build-up and dropping-down following fracture propagation.

Fig. 14 also presents a complex and an unexpected small overlapping between the upper and lower wall surfaces of the larger aperture after these two fractures intersect. This is because the pressure in the smaller aperture is always higher than the pressure in the lower portion of the larger aperture. The pressure tends to close the lower part of the larger aperture. This narrow aperture in the lower portion of the larger fracture also prevents the larger fracture from propagating at its lower tip.

Remark II. We underline that the majority of literature in modeling hydraulic fracturing problems focuses on the verification of numerical algorithms using a single and symmetric crack model and it is little reported in solving unsymmetric or multiple crack problems within the implicit formulation (standard method). In [23], to avoid potential non-convergent (the Newton iteration) issues, a hard and complex hydraulic fracture in varying its propagation direction in a medium with a heterogeneous stress distribution was simulated using the explicit finite element method. It is important to note that our effort in solving this hard two-natural hydraulic fracture problem is invested using the implicit method, a traditionally preferred computational framework. Three interested modes of crack interaction from this two nature fracture problem include crossing, arrest, and opening and they are very difficult to simulate within a coupled framework of fluid and solid fields using the implicit method. For examples, we evaluate that seeing from Fig. 8, (a) just before the two fractures connect each other, one or two elements left in the crack path of the smaller aperture would undergo high stresses; (b) just after the two fractures connect, both fluid pressure in two apertures and stresses around crack tips exhibit an abrupt change; and (c) the turning of fracture

direction toward the vertical for the larger fracture. Furthermore, the essence of the cohesive models regulates a softening behavior of materials at their failure stages. All these just discussed physics events or scenarios may bring challenges for the implicit numerical method with regard to the instability issue. By successfully solving this two nature fracture problem, we demonstrate that our proposed DG method as well as the IIPG formulation may provide a potential robust implicit computational framework in modeling of complex multiple hydraulic fracture problems.

Finally, we discuss some limitations of this work. First, our DG interfaces have to be predefined along potential paths of crack propagation. For general crack propagation problems, crack paths are unknown and become a part of solutions. In solving this two fracture problem, to identify the possible crack paths, we adopt the trial-error method to run several times. This is not efficient as the problem has to be completely resolved in each run. To greatly improve the efficiency, it is highly expected to incorporate an automatic re-meshing or rezoning solver into the proposed DG framework where crack paths are instantaneously updated within a time step. However, developing such robust remeshing solvers depend on not only efficient automatic 3D remeshing solvers themselves but also robust mapping algorithms for state variables from the previous mesh to the current mesh especially for the cases of materials involving softening or undergoing plastic deformation. Second, an overlapping occurs in our solutions case and contact models should be included in the model. However, the development of efficient automatic re-meshing DG solvers and the incorporation of contact models is out of the scope of this work.

6. Conclusion

In this work, we perform a consistent, fully implicit, and fully coupled hybrid DG/CG finite element formulation to model a large crack opening for hydraulic fracturing in porous media governed by coupled three field equations including the solid, bulk fluid, and fluid in fracture apertures resulting from fracture propagation. The contribution of fracture aperture pressure to tangent modulus of the solid equation in the solver is taken into account for better modeling of high fluid pressure injection. Specifically, we enhance our existing DG data structures to easily accommodate the isolated 3D fracture middle surfaces through associating them with DG elements. By performing the operation of grouping and breaking CG meshes, DG methods provide an efficient alternative to construct interface elements for fracture events in porous media. We had verified our IIPG formulation and implementation KGD. Finally, we demonstrate a good performance of the proposed DG method by modeling fracking in an oil/gas reservoir containing two nature fractures.

Declaration of competing interest

The authors declare that they have no known competing financial interests or personal relationships that could have appeared to influence the work reported in this paper.

Acknowledgments

Author Ruijie Liu acknowledges funding support for this research from NSF Computational Mathematics Program under award number: DMS-1911325 and author Mary Wheeler acknowledges funding support for this research from NSF Computational Mathematics Program under award number: DMS-1911320.

Appendix. Linearization for coupled three-field equation

We briefly summarize the linearized results for the solid phase equation and the bulk fluid flow equation in Eq. (22) as most linearized results for these two equations can be borrowed from [44,51]. We now summarize a

few important material time derivatives derived in [44,51] to facilitate our derivations below:

$$\begin{cases} \dot{\overline{\delta \boldsymbol{u}}} = \boldsymbol{0}; \\ \dot{\overline{\delta \boldsymbol{p}}} = \boldsymbol{0}; \\ \dot{\overline{\boldsymbol{dv}}} = \boldsymbol{trace(l)dv}; \\ \dot{\overline{\boldsymbol{\epsilon}_v}} = \boldsymbol{trace(l)}; \\ \dot{\overline{\nabla(\delta \boldsymbol{u})}} = -\nabla(\delta \boldsymbol{u})\boldsymbol{l}; \\ \dot{\overline{\nabla(\delta \boldsymbol{p})}} = -\boldsymbol{l}^T \nabla(\delta \boldsymbol{p}); \\ \dot{\overline{\nabla(\boldsymbol{p})}} = \nabla \dot{\boldsymbol{p}} - \boldsymbol{l}^T \nabla \boldsymbol{p}; \\ \dot{\overline{\boldsymbol{ds}}} = (\boldsymbol{l}_s \boldsymbol{n}) \cdot \boldsymbol{n} \boldsymbol{ds}; \\ \dot{\overline{\mathbf{ds}}} = \boldsymbol{l}_s \mathbf{ds} = \boldsymbol{l}_s \boldsymbol{n} \boldsymbol{ds} \end{cases} \tag{33}$$

where $\boldsymbol{l}$ is the rate of deformation gradient, $\boldsymbol{n}$ is the normal vector of an interface, s in bold is the vector form of a face, an $\boldsymbol{l}_s$ is further derived as follows:

$$\boldsymbol{l}_s = \boldsymbol{trace(l)I} - \boldsymbol{l}^T. \tag{34}$$

where $\boldsymbol{I}$ is the second-order identity tensor.

(a) Linearization on Fracture Flow Equation

Taking the material time derivative for the third equation in Eq. (22) and noting that aperture thickness $\boldsymbol{w_a}$ is replaced by the displacement jump, we have the following results:

$$\begin{aligned} \dot{\overline{\mathcal{R}^w \boldsymbol{a}(\boldsymbol{w_a}, \boldsymbol{p}, \delta \boldsymbol{p})}} = \quad & \{\int_{S_a} \tfrac{1}{\Delta t}[\Delta \dot{\boldsymbol{u}}_R - \Delta \dot{\boldsymbol{u}}_L]\delta \boldsymbol{p} \cdot \boldsymbol{ds} \\ & + \int_{S_a} \tfrac{1}{\Delta t}[\Delta \boldsymbol{u}_R - \Delta \boldsymbol{u}_L]\delta \boldsymbol{p} \cdot \dot{\overline{\mathbf{ds}}}\} \\ & + \{\boldsymbol{int}_{S_a} \dot{\boldsymbol{D}}^a \nabla \boldsymbol{p} \cdot \nabla(\delta \boldsymbol{p}) \boldsymbol{ds} + \int_{S_a} \boldsymbol{D}^a \dot{\overline{\nabla \boldsymbol{p}}} \cdot \nabla(\delta \boldsymbol{p}) \boldsymbol{ds} \\ & + \int_{S_a} \boldsymbol{D}^a \nabla \boldsymbol{p} \cdot \dot{\overline{\nabla(\delta \boldsymbol{p})}} \boldsymbol{ds} + \int_{S_a} \boldsymbol{D}^a \nabla \boldsymbol{p} \cdot \nabla(\delta \boldsymbol{p}) \dot{\overline{\boldsymbol{ds}}}\} \\ & - \{\int_{S_a} \boldsymbol{Q}_a[\dot{\boldsymbol{u}}_R - \dot{\boldsymbol{u}}_L]\delta \boldsymbol{p} \cdot \mathbf{ds} + \int_{S_a} \boldsymbol{Q}_a[\boldsymbol{u}_R - \boldsymbol{u}_L]\delta \boldsymbol{p} \cdot \dot{\overline{\mathbf{ds}}}\} \end{aligned} \tag{35}$$

Inserting the material time derivatives of the variables listed in Eq. (33) into Eq. (35), we linearize the fracture flow equation as follows:

$$\begin{aligned} \dot{\overline{\mathcal{R}^w \boldsymbol{a}(\boldsymbol{w_a}, \boldsymbol{p}, \delta \boldsymbol{p})}} = \quad & \{\int_{S_a} (\tfrac{1}{\Delta t}[\Delta \dot{\boldsymbol{u}}_R - \Delta \dot{\boldsymbol{u}}_L]) \cdot (\boldsymbol{tracel I} - \boldsymbol{l}^T) \boldsymbol{n}^L \\ & + \tfrac{d\boldsymbol{D}^a}{d\boldsymbol{w_a}}[\boldsymbol{u}^R - \boldsymbol{u}^L] \cdot \boldsymbol{n}^L \nabla \boldsymbol{p} \cdot \nabla(\delta \boldsymbol{p}) \\ & + (\boldsymbol{l}_s \boldsymbol{n}^L \otimes \boldsymbol{n}^L - \boldsymbol{l}^T - \boldsymbol{l}) \boldsymbol{q_a} \cdot \nabla(\delta \boldsymbol{p}) \\ & - \boldsymbol{Q}_a[\boldsymbol{u}^R - \boldsymbol{u}^L] \cdot (\boldsymbol{l}_s \boldsymbol{n}^L) \delta \boldsymbol{p} \\ & - \boldsymbol{Q}_a[\dot{\boldsymbol{u}}^R - \dot{\boldsymbol{u}}^L] \cdot (\boldsymbol{n}^L \delta \boldsymbol{p}) \boldsymbol{ds}\} \\ & + \int_{S_a} \boldsymbol{D}^a \nabla \dot{\boldsymbol{p}} \cdot \nabla(\delta \boldsymbol{p}) \boldsymbol{ds} \end{aligned} \tag{36}$$

where $\frac{d\boldsymbol{D}^a}{d\boldsymbol{w_a}}$ refers to take a derivative for the local third order conductivity tensor defined in Eq. (11) with respect to $\boldsymbol{w_a}$. It should be noted that in Eq. (36) the geometrical effect only contributes the coupling tangent modulus, and both the fracture $\boldsymbol{w_a}$ and the injection rate $\boldsymbol{Q_a}$ contribute the coupling modulus.

(b) Linearization on Equation for Fluid Flow in Bulk Matrix

We assume that the material parameters as well as the flow flux on the boundaries and the source flow rate are constant during injection. Performing the material time derivatives for the second equation in Eq. (22) for fluid flow in the bulk matrix and inserting $\boldsymbol{q} = -\boldsymbol{K}\nabla \boldsymbol{p}$ in this equation, we have:

$$\begin{aligned}
\overline{\mathcal{R}^p(\boldsymbol{u}, \boldsymbol{p}, \delta \boldsymbol{p})}^{\cdot} = \quad & \{\int_{\Omega/\Omega_a} \tfrac{\alpha}{\Delta t} \overline{\Delta \epsilon_v}^{\cdot} \delta \boldsymbol{p} d\boldsymbol{v} + \int_{\Omega/\Omega_a} \tfrac{\alpha}{\Delta t} \Delta \boldsymbol{\epsilon}_v \delta \boldsymbol{p} \overline{d\boldsymbol{v}}^{\cdot}\} \\
& + \{\int_{\Omega/\Omega_a} \tfrac{1}{M\Delta t} \overline{\Delta \boldsymbol{p}}^{\cdot} \delta \boldsymbol{p} d\boldsymbol{v} + \int_{\Omega/\Omega_a} \tfrac{1}{M\Delta t} \Delta \boldsymbol{p} \delta \boldsymbol{p} \overline{d\boldsymbol{v}}^{\cdot}\} \\
& + \{\int_{\Omega/\Omega_a} \boldsymbol{K} \overline{\nabla \boldsymbol{p}}^{\cdot} \cdot \nabla \delta \boldsymbol{p} d\boldsymbol{v} \\
& + \int_{\Omega/\Omega_a} \boldsymbol{q} \cdot \overline{\nabla(\delta \boldsymbol{p})}^{\cdot} d\boldsymbol{v} + \boldsymbol{q} \cdot \nabla(\delta \boldsymbol{p}) \overline{d\boldsymbol{v}}^{\cdot}\} \\
& - \{\int_{S_I} \boldsymbol{K} \{\overline{\nabla \boldsymbol{p}}^{\cdot}\} \cdot \boldsymbol{n}^L [\delta \boldsymbol{p}] d\boldsymbol{s} + \int_{S_i} \{\boldsymbol{q}\} \cdot \overline{\mathbf{ds}}^{\cdot} [\delta \boldsymbol{p}]\} \\
& + \boldsymbol{\beta} \delta_{pp} \tfrac{k}{\mu \sqrt{A}} \int_{S_I} [\dot{\boldsymbol{p}}] \cdot [\delta \boldsymbol{p}] d\boldsymbol{s} \\
& - \int_{\Gamma^q} \boldsymbol{t}_q \delta \boldsymbol{p} \overline{d\boldsymbol{s}}^{\cdot} - \int_{\Omega/\Omega_a} \boldsymbol{s}_q \delta \boldsymbol{p} \overline{d\boldsymbol{v}}^{\cdot}
\end{aligned} \tag{37}$$

Applying the material time derivatives of $\overline{\nabla \boldsymbol{p}}^{\cdot}$ and $\overline{\nabla(\delta \boldsymbol{p})}^{\cdot}$ as well as others in Eq. (33), we linearize the bulk flow equation as follows:

$$\begin{aligned}
\overline{\mathcal{R}^p(\boldsymbol{u}, \boldsymbol{p}, \delta \boldsymbol{p})}^{\cdot} = \quad & \{\int_{\Omega/\Omega_a} [\tfrac{\alpha(1+\Delta \epsilon_v) + \Delta p/M - s_a \Delta t}{\Delta t} \boldsymbol{trace}(\boldsymbol{l}) \delta \boldsymbol{p} \\
& + \boldsymbol{q}(\boldsymbol{l}^T - \boldsymbol{trace}(\boldsymbol{l}) \boldsymbol{I}) \cdot \nabla(\delta \boldsymbol{p})] d\boldsymbol{v} - \int_{S_I} \{\boldsymbol{q}\} \cdot (\boldsymbol{ls} - \boldsymbol{l}) \boldsymbol{n}^L d\boldsymbol{s}\} \\
& + \int_{\Omega/\Omega_a} \tfrac{1}{M\Delta t} \dot{\boldsymbol{p}} \delta \boldsymbol{p} d\boldsymbol{v} \\
& + \int_{\Omega/\Omega_a} \boldsymbol{K} \nabla \dot{\boldsymbol{p}} \cdot \nabla(\delta \boldsymbol{p}) d\boldsymbol{v} \\
& + \boldsymbol{\beta} \delta_{pp} \tfrac{k}{\mu \sqrt{A}} \int_{S_I} [\dot{\boldsymbol{p}}] \cdot [\delta \boldsymbol{p}] d\boldsymbol{s} \\
& - \int_{\Gamma^q} (\boldsymbol{l}_s \boldsymbol{n}) \cdot \boldsymbol{n} t_q \delta \boldsymbol{p} d\boldsymbol{s}
\end{aligned} \tag{38}$$

where all terms in the curly brace are related to the coupling of the solid and bulk fluid fields.

(c) Linearization on Solid Phase Equation

We introduce the Truesdell stress rate as follows:

$$\overline{\boldsymbol{\sigma}''}^{\cdot} = \boldsymbol{\sigma}''^{o} + \boldsymbol{l}\boldsymbol{\sigma}'' + \boldsymbol{\sigma}'' \boldsymbol{l}^T - \boldsymbol{trace}(\boldsymbol{l}) \boldsymbol{\sigma}'' \tag{39}$$

where $\boldsymbol{\sigma}''^{o}$ is the objective stress. Using Eq. (39), we first linearize the major DG term of $\int_{S_I} \{\boldsymbol{\sigma}'' \boldsymbol{n}^L\} \cdot [\delta \boldsymbol{u}] d\boldsymbol{s}$ in the first residual equation in Eq. (22) as follows:

$$\begin{aligned}
& \int_{S_I} \{\overline{\boldsymbol{\sigma}''}^{\cdot} \boldsymbol{n}^L\} \cdot [\delta \boldsymbol{u}] d\boldsymbol{s} + \int_{S_I} \{\boldsymbol{\sigma}'' \overline{d\boldsymbol{s}}^{\cdot}\} \cdot [\delta \boldsymbol{u}] = \\
& \int_{S_I} \{(\boldsymbol{\sigma}''^{o} + \boldsymbol{l}\boldsymbol{\sigma}'' + \boldsymbol{\sigma}'' \boldsymbol{l}^T - \boldsymbol{trace}(\boldsymbol{l}) \boldsymbol{\sigma}'') \boldsymbol{n}^L\} \cdot [\delta \boldsymbol{u}] d\boldsymbol{s} + \int_{S_I} \{\boldsymbol{\sigma}''\} \boldsymbol{l}_s \boldsymbol{n}^L d\boldsymbol{s} \cdot [\delta \boldsymbol{u}] \\
& = \int_{S_I} \{\boldsymbol{\sigma}''^{o}\} \boldsymbol{n}^L d\boldsymbol{s} \cdot [\delta \boldsymbol{u}] d\boldsymbol{s} + \int_{S_I} \{\boldsymbol{l}\boldsymbol{\sigma}''\} \boldsymbol{n}^L \cdot [\delta \boldsymbol{u}] d\boldsymbol{s} \\
& = \int_{S_I} \{\boldsymbol{\mathcal{C}} \tfrac{\boldsymbol{l} + \boldsymbol{l}^T}{2}\} \boldsymbol{l}_s \boldsymbol{n}^L d\boldsymbol{s} \cdot [\delta \boldsymbol{u}] + \int_{S_I} \{\boldsymbol{l}\boldsymbol{\sigma}''\} \boldsymbol{n}^L \cdot [\delta \boldsymbol{u}] d\boldsymbol{s}
\end{aligned} \tag{40}$$

where $\mathcal{C}$ can be the fourth-order material elasticity tensor for continuous fields or can be easily derived for the cohesive model shown in Fig. 3 for fracture failure. The remaining terms in the first residual equation in Eq. (22) are the same as those for the continuous finite element formulation, which were linearized in [51]. For the final IIPG formulation for the solid phase, we add the DG results in Eq. (40) into the CG results given in [51] as follows:

$$\begin{aligned}\dot{\overline{\mathcal{R}^u(\boldsymbol{u}, p, \delta\boldsymbol{u})}} = \quad & \int_{\Omega/\Omega_a}\{[\mathcal{C}\tfrac{(l+l^T)}{2} + l\sigma'' + \sigma''l^T \\ & +\alpha\dot{p}I - \alpha trace(l)pI]\} : \nabla(\delta\boldsymbol{u})dv \\ & -\int_{S_I}\{(\mathcal{C}\tfrac{(l+l^T)}{2} + l\sigma'')n^L\}\cdot[\delta\boldsymbol{u}]ds \\ & +\beta\delta_{pu}\tfrac{G}{\sqrt{A}}\int_{S_I}[\dot{\boldsymbol{u}}]\cdot[\delta\boldsymbol{u}]ds \\ & -\int_{\Gamma^{t/a}} l_s t_s\cdot\delta\boldsymbol{u}ds + \int_{\Gamma^a} p_a(l_s n)\cdot\delta\boldsymbol{u}ds.\end{aligned} \tag{41}$$

where we underline that the last term of $\int_{\Gamma^a} p_a(l_s n)\cdot\delta\boldsymbol{u}ds$ in Eq. (41) is to take into account the contribution from the fluid injection pressure in apertures.

For crack opening case where the cohesive law is enforced, we list the linearization result of Eq. (23) as follows:

$$\begin{aligned}\dot{\overline{\mathcal{R}^u(\boldsymbol{u}, p, \delta\boldsymbol{u})}} = \quad & \int_{\Omega/\Omega_a}\{[\mathcal{C}\tfrac{(l+l^T)}{2} + l\sigma'' + \sigma''l^T \\ & +\alpha\dot{p}I - \alpha trace(l)pI]\} : \nabla(\delta\boldsymbol{u})dv \\ & -\int_{S_I}\tfrac{\partial T}{\partial[u]}[\dot{\boldsymbol{u}}]\cdot[\delta\boldsymbol{u}]ds \\ & -\int_{\Gamma^{t/a}} l_s t_s\cdot\delta\boldsymbol{u}ds + \int_{\Gamma^a} p_a(l_s n)\cdot\delta\boldsymbol{u}ds.\end{aligned} \tag{42}$$

Finally, by replacing the spatial velocity field v by the incremental displacement $\Delta\boldsymbol{u}$, $\dot{\boldsymbol{u}}$ by $\Delta\boldsymbol{u}$, and $\dot{p}$ by Δp in Eqs. (41), (42), and (36), the tangent stiffnesses for all three field equations as well as their coupling stiffness can be written out for a DG code implementation. Examples for these tangent stiffness templates can be found in [44,51].

References

[1] J. Geertsma, F. De Klerk, A rapid method of predicting width and extent of hydraulically induced fractures, J. Pet. Technol. 21 (1969) 1571–1581.
[2] T. Perkins, L. Kern, Widths of hydraulic fractures, J. Pet. Technol. 13 (1961) 937–949.
[3] R. Nordgren, Propagation of a vertical hydraulic fracture, Old SPE J. 12 (1972) 306–314.
[4] S. Khristianovic, Y. Zheltov, Formation of vertical fractures by means of highly viscous fluids, in: Proceedings of the 4th World Petroleum Congress, Vol. 2, Rome, 1955, pp. 579–586.
[5] J. Adachi, E. Detournay, Plane strain propagation of a hydraulic fracture in a permeable rock, Eng. Fract. Mech. 75 (2008) 4666–4694.
[6] A. Bunger, E. Detournay, D. Garagash, Toughness-dominated hydraulic fracture with leak-off, Int. J. Fract. 134 (2005) 175–190.
[7] E. Detournay, Propagation regimes of fluid-driven fractures in impermeable rocks, Int. J. Geomech. 4 (2004) 35–45.
[8] D. Garagash, Plane-strain propagation of a fluid-driven fracture during injection and shut-in: asymptotics of large toughness, Eng. Fract. Mech. 74 (2007) 456–481.
[9] S. Mitchell, R. Kuske, A. Peirce, An asymptotic framework for the analysis of hydraulic fractures: The impermeable case, J. Appl. Mech. 74 (2007) 365–372.
[10] S. Mitchell, R. Kuske, A. Peirce, An asymptotic framework for finite hydraulic fractures including leak-off, Int. J. Solids Struct. 39 (2002) 6311–6337.
[11] A. Savitski, E. Detournay, Propagation of a penny-shaped fluid-driven fracture in an impermeable rock: asymptotic solutions, Int. J. Solids Struct. 39 (2002) 6311–6337.
[12] J. Hu, D. Garagash, Plane-strain propagation of a fluid-driven crack in a permeable rock with fracture toughness, J. Eng. Mech. 136 (2010) 1152–1166.
[13] H. Abe, T. Mura, L. Keer, Growth-rate of a penny-shaped crack in hydraulic fracturing of rocks, J. Geophys. Res. 81 (1976) 5335–5340.
[14] X. Gao, J. Kim, Modeling of ductile fracture: significance of void coalescence, Int. J. Solids Struct. 43 (2006) 6277–6293.
[15] G.T. Camacho, M. Ortiz, Computational modelling of impactdamage in brittle materials, Int. J. Solids Struct. 33 (1996) 2899–2938.

[16] S. Li, S. Ghosh, Modeling interfacial debonding and matrix cracking in fiber reinforced composites by the extended Voronoi cell FEM, Finite Elem. Anal. Des. 43 (2007) 397–410.
[17] H.M. Inglis, P.H. Geubelle, K. Matous, H. Tan, Y. Huang, Cohesive modeling of dewetting in particulate composites: Micromechanics vs. multiscale finite element analysis, Mech. Mater. 39 (2007) 580–595.
[18] M.G. Kulkani, K. Matous, P.H. Geubelle, Coupled multi-scale cohesive modeling of failure in heterogeneous adhesives, J. Numer. Methods Eng. 84 (2010) 914–946.
[19] X.P. Xu, A. Needleman, Numerical simulations of fast crack growth in brittle solids, J. Mech. Phys. Solids 42 (1994) 1397–1434.
[20] N. Sukumar, J.E. Dolbow, N. Moïšæs, Extended finite element method in computational fracture mechanics: a retrospective examination, Int. J. Fract. 196 (2015) 186–205.
[21] C. Miehe, M. Hofacker, F. Welschinger, A phase field model for rate-independent crack propagation: Robust algorithmic implementation based on operator splits, Comput. Methods Appl. Mech. Engrg. 199 (2010) 2765–2778.
[22] L. Simoni, S. Secchi, Cohesive fracture mechanics for a multi-phase porous medium. Part I: theoretical model, Eng. Comput. 20 (2003) 675–698.
[23] P. Fu, S.M. Johnson, C.R. Carrigan, An explicitly coupled hydro-geomechanical model for simulating hydraulic fracturing in arbitrary discrete fracture networks, Int. J. Numer. Anal. Methods Geomech. 37 (2013).
[24] J. Segura, I. Carol, Coupled HM analysis using zero-thickness interface elements with double nodes. Part I: theoretical model, Int. J. Numer. Anal. Methods Geomech. 32 (2008) 2083–2101.
[25] Z. Chen, A. Bunger, X. Zhang, R. Jeffrey, Cohesive zone finite element-based modeling of hydraulic fractures, Acta Mech. Solida Sin. 22 (2009) 443–452.
[26] T. Boone, A. Ingraffea, A numerical procedure for simulation of hydraulically-driven fracture propagation in poroelastic media, Int. J. Numer. Anal. Methods Geomech. 14 (1990) 27–47.
[27] E. Sarris, P. Papanastasiou, The influence of the cohesive process zone in hydraulic fracturing modelling, Int. J. Fract. 167 (2011) 33–45.
[28] E. Sarris, P. Papanastasiou, Modelling of hydraulic fracturing in a poroelastic cohesive formation, Int. J. Geomech. 12 (2012) 160–167.
[29] B. carrier, S. Granet, Numerical modeling of hydraulic fracture problem in permeable medium using cohesive zone model, Eng. Fract. Mech. 79 (2012) 312–328.
[30] M.G. Zielonka, K.H. Searles, J. Ning, S.R. Buechler, Development and validation of fully-coupled hydraulic fracturing simulation capabilities, in: 2014 SIMULIA Community Conference, 2014.
[31] B. Lecampion, An extended finite element method for hydraulic fracture problems, Commun. Numer. Methods Eng. 22 (2009) 121–133.
[32] T. Mohammadnejad, A.R. Khoei, An extended finite elment method for hydraulic fracture propagation in deformable porous media with the cohesive crack model, Finite Elem. Anal. Des. 73 (2013) 7795–7800.
[33] J. Nitsche, Über ein Variationsprinzip zur Lösung von Dirichlet bei verwendung von teilräumen, die keinen randbedingungen unterworfen sind, Abh. Math. Univ. Hamburg 36 (1970) 9–15.
[34] J. Douglas, T. Dupont, Interior penalty procedures for elliptic and parabolic Galerkin methods, Lecture Notes in Phys. 58 (1976) 207–216.
[35] G.A. Baker, Finite element methods for elliptic equations using nonconforming elements, Math. Comp. 31 (1977) 45–59.
[36] D.N. Arnold, An interior penalty finite element method with discontinuous elements, SIAM J. Numer. Anal. 19 (1982) 742–760.
[37] B. Riviere, S. Shaw, M.F. Wheeler, J.R. Whiteman, Discontinuous Galerkin finite element methods for linear elasticity and quasistatic linear viscoelasticity, Numer. Math. 95 (2003) 347–376.
[38] C.N. Dawson, S. Sun, M.F. Wheeler, Compatible algorithms for coupled flow and transport, Comput. Methods Appl. Methods Eng. 193 (2004) 2565–2580.
[39] G.N. Wells, K. Garikipati, L. Molari, A discontinuous Galerkin formulation for a strain gradient-dependent damage model, Comput. Methods Appl. Mech. Engrg. 193 (2004) 3633–3645; Comput. Methods Appl. Mech. Engrg. 193 (2004) 3633–3645, 56 (1996) 755–760.
[40] L. Molari, G.N. Wells, K. Garikipati, F. Ubertini, A discontinuous Galerkin method for strain gradient-dependent damage: study of interpolations and convergence, Comput. Methods Appl. Mech. Engrg. 195 (2006) 1480–1498.
[41] P. Hansbo, M.G. Larson, Discontinuous Galerkin method for incompressible and nearly incompressible elasticity by nitche's methods, Comput. Methods Appl. Mech. Engrg. 191 (2002) 1895–1908.
[42] R. Liu, M.F. Wheeler, C. Dawson, A three-dimensional nodal-based implementation of a family of discontinuous Galerkin methods for elasticity, Comput. Struct. 87 (2009) 141–150.
[43] R. Liu, M.F. Wheeler, C. Dawson, R. Dean, On a coupled discontinuous/continuous Galerkin framework and an adaptive penalty scheme for poroelasticity problems, Comput. Methods Appl. Mech. Engrg. 198 (2009) 3499–3510.
[44] R. Liu, M.F. Wheeler, I. Yotov, On the spatial formulation of discontinuous Galerkin methods for finite elastoplasticity, Comput. Methods Appl. Mech. Engrg. 253 (2012) 219–236.
[45] R. Liu, Discontinuous Galerkin Finite Element Solution for Poromechanics Problem (Ph.D. dissertation), The University of Texas at Austin, 2004.
[46] R. Liu, M.F. Wheeler, C. Dawson, R. Dean, Modeling of convection-dominated thermoporomechanics problems using incomplete interior penalty Galerkin method, Comput. Methods Appl. Mech. Engrg. 198 (2009) 912–919.
[47] P. Hansbo, K. Salomonsson, A discontinuous Galerkin method for cohesive zone modelling, Finite Elem. Anal. Des. 102–103 (2015) 1–6.
[48] J. Mergheim, E. Kuhl, P. Steinmann, A hybrid discontinuous Galerkin/interface method for the computational modelling of failure, Int. J. Numer. Methods Biomed. Eng. 20 (2004) 511–519.

[49] V.P. Nguyen, Discontinuous Galerkin/extrinsic cohesive zone modeling: Implementation caveats and applications in computational fracture mechanics, Eng. Fract. Mech. 128 (2014) 37–68.
[50] L. Wu, D. Tjahjanto, G. Becker, A. Makradi, A. Je?rusalem, L. Noels, A micro-meso-model of intra-laminar fracture in fiber-reinforced composites based on a discontinuous Galerkin/cohesive zone method, Eng. Fract. Mech. 104 (2013) 162–183.
[51] R. Liu, Z. Liu,
[52] R. Liu, A. Mostafa, Z. Liu, Modeling of structural failure of zircaloy claddings induced by multiple hydride cracks, Int. J. Fract. 213 (2018) 171–191.
[53] P. Witherspoon, J. Wang, K. Iwai, J. Gale, Validity of cubic law for fluid flow in a deformable rock fracture, Water Resour. Res. 16 (1980) 1016–1024.
[54] J.T. Oden, Finite Elements of Nonlinear Continua, McGraw-Hill, New York, 1972.
[55] J.C. Simo, T.J.R. Hughes, Computational Inelasticity, Springer-Verlag, New York, 1998.
[56] A. Masud, C.L. Tham, W.K. Liu, A stabilized 3-D co-rotational formulation for geometrically analysis of multi-layered composite shells, Int. J. Comput. Mech. 26 (2000) 1–12.
[57] R. Liu, M.F. Wheeler, C.N. Dawson, R. Dean, A fast convergent rate preserving discontinuous Galerkin framework for rate-independent plasticity problems, Comput. Methods Appl. Mech. Engrg. 199 (2010) 3213–3226.
[58] Y. Kovalyshen, Fluid-Driven Fracture in Poroelastic Medium (Ph.D. thesis), University of Minnesota, 2010.
[59] E.E. Detournay, A. Cheng, J. McLennan, A poroelastic PKN hydraulic fracture model based on an explicit moving mesh algorithm, ASME J. Energy Resour. Technol. 112 (1990).